UNIVERSITY OF TEXAS ARLINGTON

MASTERS THESIS

Catalogue of Computed Pseudo-Redshifts from BATSE GRB Data

Author:
Rebecca PRONI

Supervisor:
Dr. Amir SHAHMORADI

A thesis submitted in fulfillment of the requirements
for the degree of Master of Science

in the

Computational Data Science Lab
Department of Physics

May 2020

Declaration of Authorship

I, Rebecca PRONI, declare that this thesis titled, "Catalogue of Computed Pseudo-Redshifts from BATSE GRB Data" and the work presented in it are my own. I confirm that:

- This work was done wholly or mainly while in candidature for a research degree at this University.
- Where any part of this thesis has previously been submitted for a degree or any other qualification at this University or any other institution, this has been clearly stated.
- Where I have consulted the published work of others, this is always clearly attributed.
- Where I have quoted from the work of others, the source is always given. With the exception of such quotations, this thesis is entirely my own work.
- I have acknowledged all main sources of help.
- Where the thesis is based on work done by myself jointly with others, I have made clear exactly what was done by others and what I have contributed myself.

Signed:

Date:

UNIVERSITY OF TEXAS ARLINGTON

Abstract

Faculty Name
Department of Physics

Master of Science

Catalogue of Computed Pseudo-Redshifts from BATSE GRB Data

by Rebecca PRONI

We present a catalog of the redshift estimates and probability distributions for 565 individual Short-duration Gamma-Ray Bursts (SGRBs) detected by the Burst And Transient Source Experiment (BATSE). This result is based on a careful classification and modeling of the population distribution of BATSE SGRBs in the 5-dimensional space of redshift as well as the intrinsic prompt gamma-ray emission properties: the isotropic 64ms peak luminosity, the total isotropic emission, the spectral peak energy, as well as the intrinsic duration, while taking into account the complex detection mechanism of BATSE and sample incompleteness. The underlying assumption in our modeling approach is that SGRBs trace the Cosmic Star Formation Rate convolved with plausible binary Neutron-Star merger-delay-time distributions. Our modeling approach enables us to constrain the redshifts of BATSE SGRBs for the first time, and to reconstruct the cosmic distribution map of all BATSE SGRBs in the world.

Acknowledgements

I am extremely grateful to my advisor, Dr. Amir Shahmoradi, for his invaluable help and support. I must also thank Joshua Osborne for his guidance and help. I would also like to thank all of my fellow group members at the Computational Data Science lab for their support. Thanks also to Dr. Qiming Zhang, for his help and guidance during my years at UTA. Finally, I would like to thank my parents, for their unwavering support during my graduate years.

Contents

List of Figures

List of Tables

List of Abbreviations

BAND	GRB Model
BATSE	Burst And Transient Source Experiment
BETA	GRB Model with Fixed β
CGRO	Compton Gamma-Ray Observatory
GRB	Gamma Ray Bursts
LAD	Large Area Detector
LGRB	Long Gamma Ray Bursts
S/N	Signal-to-Noise Ratio
SD	Spectroscopy Detectors
SGRB	Short Gamma Ray Bursts

Physical Constants

Astronomical Unit	$\mathrm{au} = 149\,597\,870\,700\,\mathrm{m}$(exact)
Speed of Light	$c_0 = 2.997\,924\,58 \times 10^{8}\,\mathrm{m\,s^{-1}}$ (exact)
Hubble Constant	$H = 71$ km/s/MPc
Parsec	$pc = 6480000/\pi$ astronomical units
Dark Energy Density	$\Omega_{\mathrm{DE}} = 0.7$
Dark Matter Density	$\Omega_{\mathrm{DM}} = 0.3$

List of Symbols

A	Amplitude	-
α	BAND Low-Energy Spectral Index; Electron Deflection Angle	-
β	BAND High-Energy Spectral Index	-
α_{eff}	Effective α	-
c	Speed of Light	m/s
e	Electron Charge	eV
E_{iso}	Total Isotropic Emission	ergs
L_{iso}	Isotropic Peak Luminosity	erg/s
$E_{\mathrm{p},z}$	Rest-Frame Time-Integrated Spectral Peak Energy	ergs
T_{90}	Observer-Frame Time Duration	seconds
$T_{90,z}$	Rest-Frame Time Duration	seconds
S_{bol}	Bolometric Fluence	erg/cm^2
P_{bol}	Bolometric Peak Flux	photons^{-1} cm^{-2}
E_{p}	Observed Peak Energy	keV
$\dot{\zeta}$	Co-moving Rate Density	-

Chapter 1

Introduction

1.1 Gamma-ray Bursts

Gamma-ray bursts (GRBs) are extremely energetic flashes of gamma-ray photons and the brightest cataclysmic electromagnetic events known to occur in the universe. These electromagnetic events take the shape of a narrow cone made up of gamma-rays and are estimated to release a total amount of energy in the range of 10^{50}-10^{51} ergs. GRBs are believed to be extremely energetic since most GRBs appear to occur billions of lightyears away from Earth, implying that they would have to have a lot of energy to be detected on Earth from so far away. They are also extremely rare, occurring on the order of a few per galaxy per million years (Podsiadlowski et al., 2004).

The discovery of gamma-ray bursts happened serendipitously, on July 2, 1967, by the U.S. Vela satellites (Klebesadel, Strong, and Olson, 1973). Originally made to detect covert nuclear testing, the Vela satellites were also capable of detecting gamma-ray bursts originating from space. On July 2nd, a signal was detected that did not resemble that produced from a nuclear weapon. The information of the GRB detection was finally declassified and published in 1973 in the paper *Observations of Gamma-Ray Bursts of Cosmic Origin* by Ray Klebesadel, Roy Olson, and Ian Strong of the University of California and the Los Alamos Scientific Laboratory. These findings were also presented by Klebesadel at the 140^{th} meeting of the American Astronomical Society.

The exact creation method of GRBs and their progenitors remain uncertain, despite the many studies conducted in the past few decades. However some theories are widely accepted, including the hypothesis that the intense radiation is released by a supernova or superluminous supernova as a high mass star implodes to form a black hole or neutron star. Another progenitor of gamma-ray bursts is thought to be the merger of neutron stars, or a neutron star and a black hole.

GRBs typically comprise of an initial burst of high energy photons followed by an *afterglow*. The afterglow of a GRB is a slowly fading emission of lower energy (longer wavelength) gamma-rays following the initial burst of gamma-rays. This is caused by the burst ejecta colliding with interstellar gas. Since the afterglow is lower energy, it is harder to detect than the initial high energy burst. It was first observed in 1997 by the BeppoSAX satellite when it detected GRB 970228. Deep imaging observed a distant host galaxy, pinpointed by the optical afterglow. Spectral analysis revealed a redshift of z = 0.835, which indicates that the burst is approximately 6 billion light-years away from Earth.

The time profiles of GRBs are extremely diverse, with an event lasting anywhere from milliseconds to minutes (Gerald J Fishman and C. A. Meegan, 1995). Because the time profiles are so diverse, GRBs are broadly classified into two groups based on their duration, with approximately 2 seconds used as a dividing line (Kouveliotou et al., 1993). *Short Gamma-Ray Bursts* (SGRBs) last for less than two seconds, and *Long Gamma-Ray Bursts* (LGRBs) last for longer than 2-3 seconds. LGBRs are also typically followed by an afterglow emission, which lasts much longer than the bursts themselves. Afterglows are not unique to LGBRs but are more common with them. A third group, *ultra-long gamma-ray bursts*, have also been suggested to categorize GRBs that last for longer 10,000 seconds, but some people think the data is too inconclusive for this to constitute a category.

1.2 Classification

1.2.1 Short Gamma-Ray Bursts (SGRBs)

SGRBs are categorized as GRBs that last for less than approximately 2-3 seconds. This subclass of GRBs accounts for approximately 30% of detected GRBs. The progenitors that cause these GRBs are thought to be the merger of two neutron stars or the merger of a neutron star with a black hole (Nakar, 2007).

No afterglow following the SGRB was detected until 2005 due to the difficultly in detecting afterglow radiation since it has a longer wavelength than the initial burst. Before this, the afterglow was only detected for Long Gamma-Ray Bursts. Gamma-Ray burst GRB 050709 (detected on May 9th 2005) was the first short GRB with an afterglow to be observed (Tanvir et al., 2013, Edo Berger, Fong, and Chornock, 2013).

This provides more support for theory that SGRBs are caused by neutron star mergers or a neutron star and black hole merger, as opposed to being caused by supernovas. More SGRB afterglows have been detected since then and localized to regions of space where there is little star formation and old binary stars are thought to be located. This is relevant because these GRBs are not associated with supernovae (Joshua S Bloom, J. Prochaska, et al., 2006).

The average duration of these events is 0.2 seconds, which suggests a relatively (in stellar terms) small diameter of 0.2 light seconds, or 60,000 km. The observation of X-ray flashes lasting minutes to hours after an SGRB is consistent with the absorption of small particles, like the remnants of a neutron star by a black hole.

The main part of the star is absorbed by the black hole which causes the initial SGRB, then the remnants of the neutron star are absorbed more slowly over a longer period of time (relative to the initial absorption). This causes the afterglow, and the smaller size of the neutron star particles being absorbed is also why the afterglow is lower energy (longer wavelength) than the initial SGRB.

1.2.2 Long Gamma-Ray Bursts (LGRBs)

LGRBs are categorized as gamma-ray bursts that last longer than approximately 2-3 seconds. These GRBs are generated when massive stars die and become supernovas before they then collapse into a black hole (Woosley and J. Bloom, 2006). After this occurs a series of relativistically expanding shells are ejected.

It is believed that shock waves are formed when two expanding shells of relativistic material coming out of the progenitor of the GRB collide with each, dissipating some of their kinetic energy. This causes relativistic electrons to accelerate and cause the GRB prompt gamma-ray emission. When the outward traveling shells encounter interstellar medium they undergo another series of shock waves (Katz, 1993,

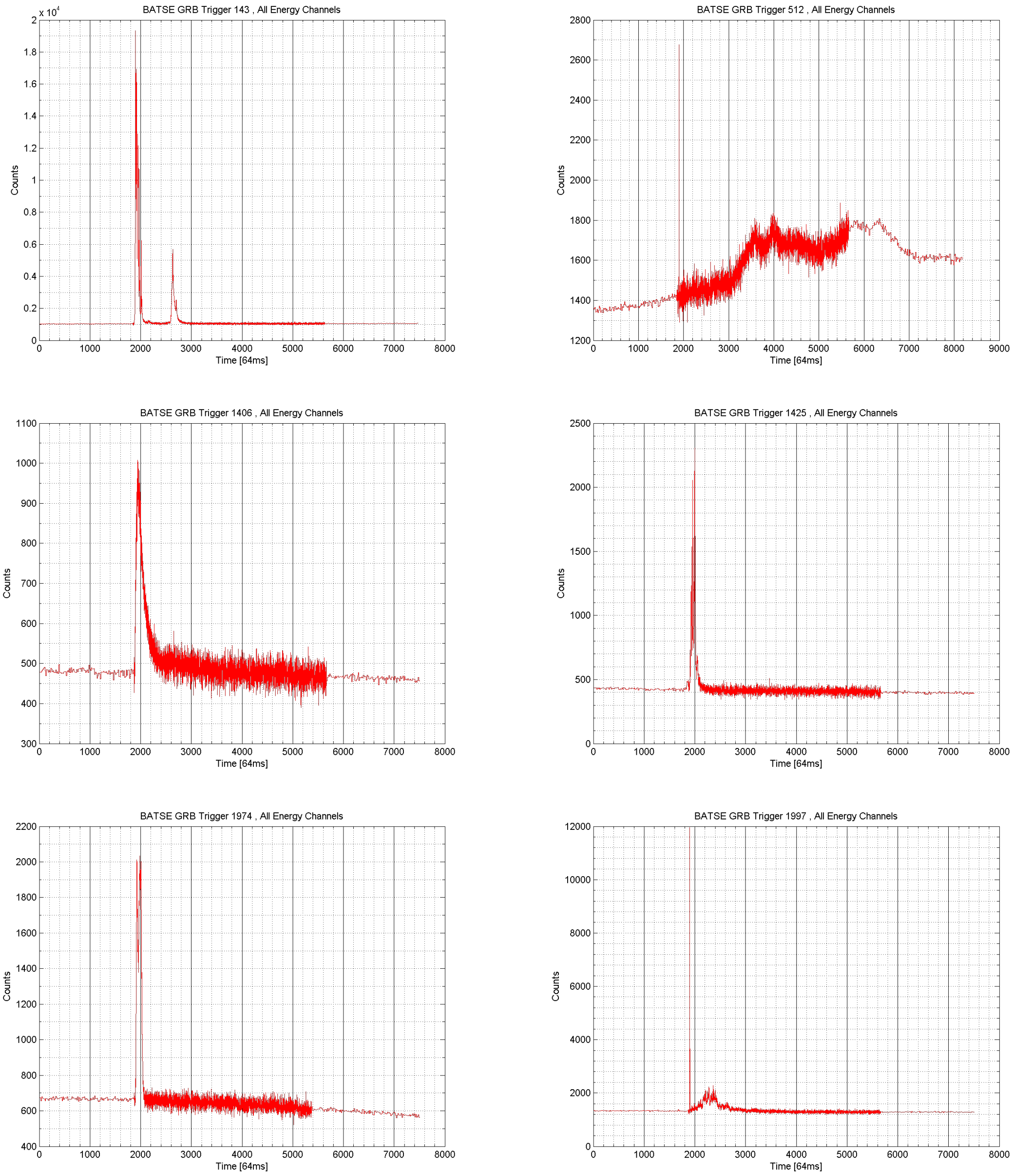

FIGURE 1.1: An illustration of six different GRB light curves. The y-axis is the counts of photons detected in 64 ms intervals, while the x-axis is the time in seconds. Data is taken from the Current BATSE Catalog.

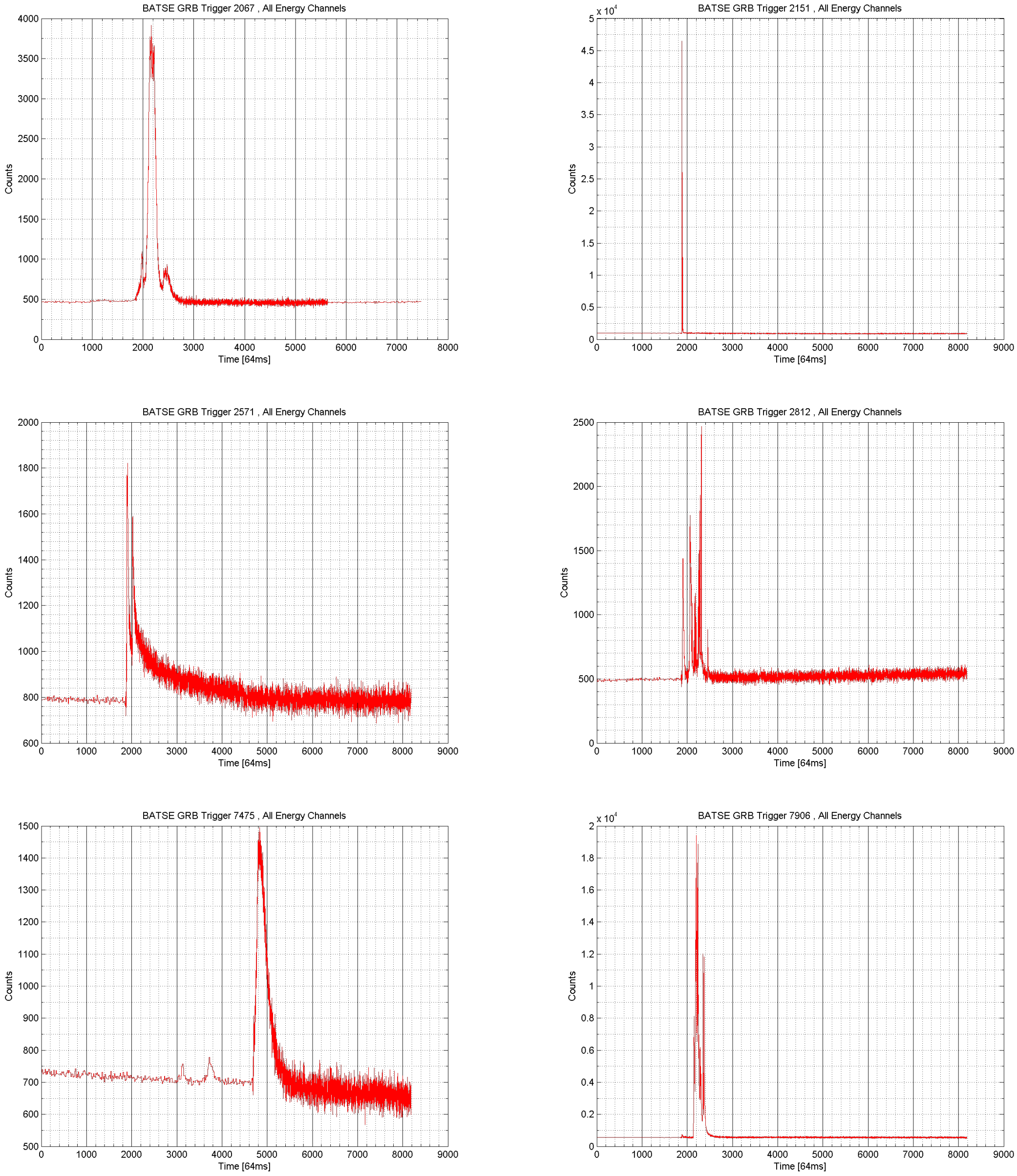

FIGURE 1.2: An illustration of six different GRB light curves. The y-axis is the counts of photons detected in 64 ms intervals, while the x-axis is the time in seconds. Data is taken from the Current BATSE Catalog.

Tavani, 1996). The afterglow emission is thought to be the result of synchrotron radiation caused by the accelerated electrons traveling through a magnetic field behind the shock wave.

LGRBs comprise approximately 70% of observed GRB events. Because they are relatively common and give the brightest afterglows, they have been observed in much greater detail than SGRBs. Most LGRBs that have been studied are linked to galaxies with rapid star formation. The observations of long afterglows at high redshift is also consistent with this (Pontzen et al., 2010). Many LGRBs have also been linked to core-collapse supernovae and thus the death of massive stars.

1.2.3 Ultra-Long Gamma-Ray Bursts

Ultra-Long Gamma-Ray Bursts last for more than 10,000 seconds, falling at the tail end of the long GRB distribution. The progenitors of these GRBs are hypothesized to be the birth of a magnetar, the collapse of a blue supergiant star, or a tidal disruption event, so a separate class has been proposed for these events. The defining characteristics of these events is the ultra-long durations of their gamma-ray emissions, and only a few have been identified to date. Of these events, the most studied ones are GRB 111209A and GRB 101225A. The low detection of these events might be ascribed to the detector sensitivity not being attuned to ultra-long-duration events, rather than indicative of the true frequency of Ultra-long gamma-ray bursts. As shown by Zhang et al., 2014 the existing evidence for a separate ultra-long GRB population with a new type of progenitor is inconclusive, and further multi-wavelength observations are needed to draw a firmer conclusion.

1.3 Energetics and Beaming

Despite their immense distances from Earth, gamma-ray bursts are very bright. The bolometric flux of an average LGRB is comparable to that of a bright star within the Milky Way galaxy, despite being a distance of billions of light-years away. Most of the energy of a GRB is released in the form of high energy gamma radiation, although some GRBs also release energy in lower frequency wavelengths, such as those in the visible light spectrum. For example, GRB 080319B, which originated 7.5 billion light-years from Earth, was accompanied by an optical counterpart with. a peak visible magnitude of 5.8, which is comparable to a dim, naked-eye star viewed in the night sky. This implies that the source is extremely energetic, within a factor of two of the rest-mass energy of the Sun, which is the energy that would be released if the Sun were to be converted entirely into radiation, assuming that the gamma-ray explosion was spherical (J. Bloom et al., 2009).

When accounting for this effect in calculating the energy released by a typical gamma-ray burst, the true energy release is calculated to be about 10^{44} J (D. A. Frail et al., 2001).

Several of the nearest GRBs have also been observed to be accompanied by supernovae. Observations of strong asymmetries in the spectra of nearby type Ic supernovae and radio observations taken long after bursts when their jets are no longer relativistic, offer additional support that the output of GRBs is focused.

The narrow jet shape of gamma-ray bursts means that most GRBs are unable to be detected on Earth since they will miss the Earth entirely. When a GRB is pointed at Earth, and therefore able to be detected, the narrow beam of energy causes the burst to appear much brighter than if it had a spherical energy emission. By observing the 'jet breaks' in afterglow light curves, the angular width of the beam can be estimated. This is done by examining the part of the light curve where the afterglow begins to fade more rapidly than its initial slow decay, which happens when the jet slows and becomes less effective at beaming its radiation. The jet angle has been observed to have significant variation, between 3 and 30 degrees (Firmani et al., 2006).

Short duration GRBs are less luminous than LGRBs and are observed to come from a less distant (lower redshift) population of space. As a population, short GRBs are less likely to be collimated than long GRBs, and the degree of beaming in SGRBs has not been accurately measured (Watson et al., 2006).

1.4 Progenitors

Gamma-ray progenitors are celestial objects that are capable of releasing high energy radiation. Gamma-ray bursts are extremely diverse, can have a duration ranging from a fraction of a second to many minutes, have highly differing spectra, and have many differing light curves. Progenitors have been theorized to be supernovae, hypernovae, accretion of matter onto neutron stars, antimatter accretion, magnetic flares on white dwarfs, rapid extraction of rotational energy from supermassive black holes, and evaporating black holes, among others.

Although many theories exist, there are at least two different progenitors of GRBs, corresponding to the two different subclasses. Long GRBs are caused by the core collapse of massive, low-metallicity stars (supernovae). Short GRBs are caused by compact binary systems of neutrons stars, or a neutron star and a black hole, merging. This was confirmed by the GW170817 observation of a kilonova and a neutron star merger (B. P. Abbott et al., 2017).

1.4.1 Long GRB Progenitors

The Collapsar Model

There is an almost universal agreement within the astrophysics community that long-duration GRBs are caused by the deaths of massive stars in supernova-like events, called hypernovae or collapsars. These events occur when very massive stars reach the end of their life cycle and have fused all the material in their cores completely to iron, at which point the star is unable to generate enough energy by fusion and collapses, forming a black hole. If the star was rotating rapidly, it is then that matter around the star's core falls towards the center and a high-density accretion disk is formed. The fall of material into the black hole causes a pair of jets to form along the rotational axis at relativistic velocities, creating a relativistic shock wave at the front, which increases as the density of the stellar matter the wave is traveling through decreases (MacFadyen, Woosley, and Heger, 2001). If there is not a thick, diffuse hydrogen envelope surrounding the star, then the jets can reach the stellar surface where it then breaks out into space, releasing much of its energy in the form of gamma-rays.

Under this theory, for long gamma-ray bursts to be formed, three special conditions must be met. First the star must be massive enough to form a black hole. Second, the star must be rotating rapidly enough to form an accretion torus that is capable of launching jets of material. Third, the star must have a low enough metallicity so that its hydrogen envelope is stripped off and the jets can reach the stellar surface.

There are two lines of evidence supporting this theory. First, GRBs have a strong association with star formation, as they are found in areas of recent star formation, which massive stars are also typically found in (Joshua S Bloom, Shrinivas R Kulkarni, and S George Djorgovski, 2002). Second, a supernova has immediately followed a GRB in several observed cases. These cases are in lower-redshift systems, as GRBs that occur in other systems are too far away for current instruments to detect them.

1.4.2 Short GRB Progenitors

Degenerate Binary Systems

Until 2007, only a few short gamma-ray bursts had been localized to a definite galactic host. These localized events demonstrate significant differences from long gamma-ray burst events. At least one SGRB was found in the star-forming central region of a galaxy and several others have been observed in areas where star formation has nearly ceased, such as the outer regions and outer halo of large elliptical galaxies. All galactic hosts of SGRBs identified so far have been at low redshift (Jason X Prochaska et al., 2006). No supernova has been observed to proceed any short GRB.

Neutron star and neutron star/black hole mergers

The generally preferred model within the astrophysical community for the progenitors of short gamma-ray bursts is the merger of two compact objects via gravitational inspiral (Blinnikov et al., 2018). The two compact objects are either two neutron stars or a neutron star and a black hole (Lattimer and Schramm, 1976).

The system loses energy over time due to gravitational radiation, and the two objects begin to spiral closer together, until eventually, they merge into one object. Right before this merger, the tidal forces of gravity will rip the neutron star (or stars) apart, liberating an immense amount of energy before the merger. This process is extremely fast, lasting within a few seconds, which accounts for the short duration of these bursts.

The distribution of short GRB host galaxies offers support for this model, as SGRBs have been observed to originate from galaxies that are relatively old with no star formation.

Magnetar giant flares

Another possible model for short gamma-ray burst is magnetar giant flares, also called megaflares or hyperflares. A magnetar is a type of neutron star that has an extremely powerful magnetic field, around the order of $10^{13} - 10^{15}$ Gauss [G]. For reference, Earth's magnetic field ranges from $0.3 - 0.6$ [G]. The decay of the magnetic field over time causes the emission of x-rays and gamma-rays along with other high-energy electromagnetic radiation.

Since the rotation of the magnetar causes the sources to repeat and the explosions have soft high-energy spectra, they can be identified as a separate class from normal gamma-ray bursts.

Tidal disruption events

A tidal disruption event occurs when a star approaches sufficiently close enough to a black hole that it is pulled apart by the tidal force from the black hole and undergoes spaghettification. If a portion of the star's mass is caught into an accretion disk around the black hole, this results in a temporary flare of electromagnetic radiation as the matter in the disk is absorbed by the black hole.

1.5 Emission Mechanisms

Gamma-ray burst emission mechanisms are theories that explain how the energy from a gamma-ray burst progenitor is converted into radiation, regardless of the nature of the progenitor. The early-time spectra and the light curves of GRBs do not resemble the radiation emitted by any familiar process.

As of 2010 there is still no generally accepted model for the mechanism by which gamma-ray bursts are converted into energy, as this process remains poorly understood. The model must be able to explain how the physical process that generates gamma-ray emission works and matches the observed characteristics such as the spectra and light curves, among other things. The model will also need to explain the high efficiencies that come from some GRBs that convert half or more of the explosion energy into gamma-rays, as well as explaining why all GRBs do not have the same efficiency (Woźniak et al., 2009).

Better understood is the nature of the afterglow emission of a GRB. The afterglow emission has a longer wavelength (typically within the range of x-ray to radio) than the initial gamma-ray burst. The energy that was released in the explosion but not converted into gamma radiation instead takes the form of energy or matter moving outward at relativistic velocities. When this matter collides with interstellar gas surrounding it this creates a relativistic shock wave that propagates into interstellar space. This may also create a second shock wave that propagates in the opposite direction as the first shock wave, into the ejected matter. Strong magnetic fields accelerate the electrons within the shock wave and radiate as synchrotron emission across most of the electromagnetic spectrum (Perna, Re'em Sari, and D. Frail, 2003). This model successfully explains the behavior of afterglows hours or days after the explosion, but has difficulty explaining the behavior of the afterglow immediately after the initial GRB.

1.5.1 Compactness problem

One problem with modeling gamma-ray bursts is what is referred to as the compactness problem. The size of the emitting region must be very small, as GRBs vary on short timescales, and if the emitting region was not small, the time delay would wipe out any short-timescale behavior. However, if the system holding the GRB progenitor is moving towards Earth at relativistic velocities, the burst is compressed in time due to the relativistic doppler effect, and as a consequence the emitting region would appear to be much smaller than its true size.

1.5.2 GRBs and internal shocks

Another constraint is imposed by the relative timescales between the total length of the GRB and the short-timescale variability, with the variability timescale often being far shorter than the total burst length. When two shells collide, the matter is flash-heated, amplifying the energy released by converting kinetic energy into the random motion of particles. The exact physical mechanisms producing the observed photons is still uncertain, but the most likely theories are inverse Compton scattering and synchrotron radiation.

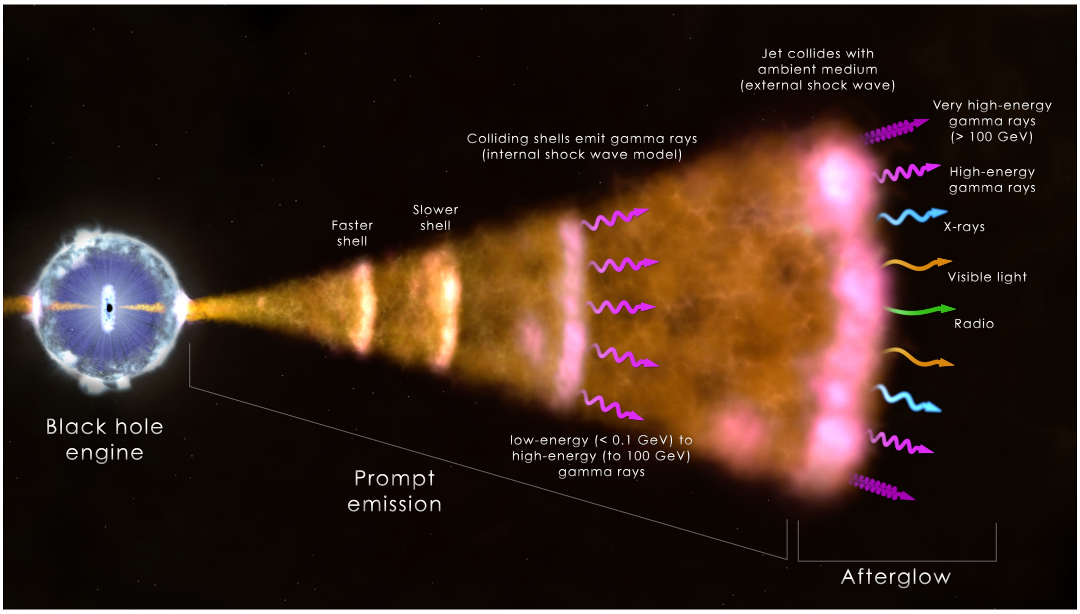

FIGURE 1.3: The emission mechanism of GRBs caused by the collapse of a massive star into a black hole. This drives a jet of particles that move out into space at nearly the speed of light. This may be caused by the jet interacting with gas near the black hole and also from collisions between fast-moving gas shells within the jet. This prompt emission will typically have a duration of a minute or less. The afterglow, caused by the leading edge of the jet interacting with its surroundings and causing an external shock wave which emits radiation across the spectrum, typically lasts from months to years. These are the most common type of short gamma-ray bursts produced.

While there has been no theory that can describe the spectrum of all gamma-ray bursts, the Band function is empirically fairly successful at fitting the spectra of most gamma-ray bursts, and is defined in Band et al., 1993 as

$$f_B(E) = \begin{cases} A\left(\frac{E}{100\mathrm{keV}}\right)^{\alpha} \exp\left(-\frac{E(2+\alpha)}{E_p}\right), & \text{if } E \leq E_c \\ A\left[\frac{(\alpha-\beta)E_p}{100(2+\alpha)}\right]^{(\alpha-\beta)} \exp(\beta-\alpha)\left(\frac{E}{100\mathrm{keV}}\right)^{\beta}, & \text{if } E \geq E_c \end{cases} \tag{1.1}$$

where

$$E_c = (\alpha - \beta)\frac{E_p}{2+\alpha} \equiv (\alpha - \beta)E_0 \tag{1.2}$$

where the parameters are the amplitude A in photons/s/keV/cm^2, the low-energy spectral index α, the high-energy spectral index β, and the peak energy E_p in keV.

1.5.3 Afterglows and external shocks

The afterglow emission is not believed to be dominated by internal shocks, unlike the GRB emission. All of the ejected matter has coalesced into a single shockwave shell traveling into the interstellar medium surrounding the star. A shock wave referred to as the 'external shock' is at the front of this shell of matter. The matter moving at relativistic speeds will then collide with the interstellar gas surrounding the star. The interstellar matter is heated to extreme temperatures as it moves across the shock wave. These particles, now relativistically moving, encounter a strong local magnetic field and are accelerated perpendicular to the magnetic field, causing them to radiate their energy via synchrotron radiation.

1.6 Current and Past GRB detection Missions

1.6.1 Discovery of the First GRB

The discovery of Gamma-Ray Bursts happened by accident, on July 2, 1967, by the U.S. Vela satellites. These satellites were initially constructed to detect secret nuclear tests in space by detecting gamma radiation pulses produced by these weapons. Four satellites made up the Vela system so that it would be possible to localize the source of any gamma-ray signals detected, and these satellites orbited above the Van Allen radiation belt at an altitude of about 105000 km. These features also made the satellites capable of detecting gamma-ray bursts originating from space. The signal detected on July 2nd did not resemble that produced from a nuclear weapon, and the light curve it produced had two peaks. Solar flares and supernovas were ruled out as a possible explanation, as none of these events had occurred at that time.

The fifth Vela satellites (Vela 5), with increased sensitivity and time resolution, was launched on May 23, 1969. It detected 12 events that did not occur at the same time as any solar flares or supernovas, some of these detections exhibiting the same double peak pattern as the initially detected signal. It was initially thought that the gamma-ray bursts may originate from specific sources within the Milky Way Galaxy. To determine the origins of GRBs, the Vela 6 satellites, launched on April 8, 1970, were deliberately launched to be on the order of 10000 km apart from the Vela 5 satellites, so that any gamma-ray events would be detected at slightly different times by different satellites. From this, 16 gamma-ray bursts were detected, randomly distributed across the sky.

The information of the GRB detection was finally declassified and published in 1973 in the paper *Observations of Gamma-Ray Bursts of Cosmic Origin* by Ray Klebesadel, Roy Olson, and Ian Strong of the University of California Los Alamos Scientific Laboratory. These findings were also presented by Klebesadel at the 140th meeting of the American Astronomical Society.

1.6.2 FERMI

The Fermi Gamma-ray Space Telescope (or 'Fermi') is a space observatory in low Earth orbit that is currently performing gamma-ray astronomy observations. It contains two scientific instruments, the Large Area Telescope (LAT) and the Gamma-ray Burst Monitor (GBM). Fermi was launched on June 11, 2008, and currently resides in orbit.

The main instrument onboard the satellite is the LAT, which is a pair-conversion gamma-ray detector with an energy range of 20 MeV to 300 GeV. The GBM is made up of 14 total scintillation detectors. Twelve of the scintillation detectors use sodium iodide crystals, giving an energy detection range of 8 KeV to 1 MeV. The remaining two scintillators use bismuth germanate crystals, giving an energy detection range of 150 KeV to 30 MeV (Atwood et al., 2009).

Along with studying gamma-ray bursts, the Fermi satellite is also searching for evaporating primordial micro black holes, probing dark matter, searching for unidentified sources and diffuse emission of gamma-rays, and studying particle acceleration in supernova remnants, pulsars, and active galactic nuclei.

1.6.3 SWIFT

The Neil Gehrels Swift Observatory, or 'Swift' (Gehrels et al., 2004), is a multiwavelength space observatory dedicated to the observation and study of gamma-ray bursts. The satellite contains three scientific instruments, the Burst Area Telescope (BAT), the X-ray Telescope (XRT), and the Ultraviolet/Optical Telescope (UVOT). Swift was launched on November 20, 2004, and currently resides in orbit.

The Swift satellite is comprised of two major telescopes: 1. The Burst Area Telescope (BAT) which is responsible for the detection of gamma-ray signals and 2. The X-ray Telescope (XRT) which is used to perform spectral analysis of the GRB afterglows and to take images of them, thus providing a more precise location of the origin of the GRB. The XRT can also observe the afterglow lightcurves for days to weeks after the event, performing long term monitoring.

1.6.4 Compton Gamma-ray Observatory

The Compton Gamma-ray Observatory (CGRO), launched in 1991, was operational for 9 years, retiring in 2000. The explicit goal of the CGRO was to detect GRBs. It contained four telescopes with the corresponding energy ranges: the Oriented Scintillation Spectrometer Experiment (OSSE) with a range of 0.05 - 10 MeV, the Imaging Compton Telescope (COMPTEL) with a range of 0.75 - 30 MeV, the Energetic Gamma-ray Experiment Telescope (EGRET) with a range of 20 MeV - 30000 MeV, and the Burst and Transient Source Experiment (BATSE) with an effective energy window of 20 - 2000 keV. The BATSE telescope is the instrument that recorded the data used in this thesis.

1.7 The Goal of This Study

Throughout its operational lifetime, BATSE triggered on 2704 GRBs. As of 2020, the BASE GRBs constitute the largest catalog of homogeneously detected GRB events in history. Despite other GRB catalogs, however, the analysis of BATSE GRB lightcurves and spectra has proven challenging partly because of the relatively low-quality and resolution of data compared to the data collected by the newer missions, but also because of missing cosmic distance information of BATSE GRBs.

The BATSE detectors operated at a time when the field of GRBs was at its infancy. Even the galactic vs. extra-galactic origins of GRBs was well evidenced toward the end of BATSE's operational lifetime. The cosmological distances of GRBs are measured by a quantity known as the *redshift*, a unit-less quantity which measures the amount of reddening of the emission or absorption spectra in the afterglows of GRBs or their host galaxies, thereby giving an indirect estimate of the distance of the GRB from the Earth. Assuming a cosmological model, this redshift information can be then converted to a *luminosity distance* which measures how far the GRB occurred from the Earth, in units of length, for example, light-years or Mega-Parsecs (MPc).

The knowledge of the redshifts of GRBs is crucial for a better understanding of their cosmological origins, their intrinsic energetics, and properties, such as duration, average emission frequency, total energy released, etc. Out of 2704 BATSE-detected GRBs, only a handful of 7 GRBs have measured redshifts. Thus to increase the usage of this vast catalog of GRBs it is essential to somehow estimate the unknown redshifts of GRBs.

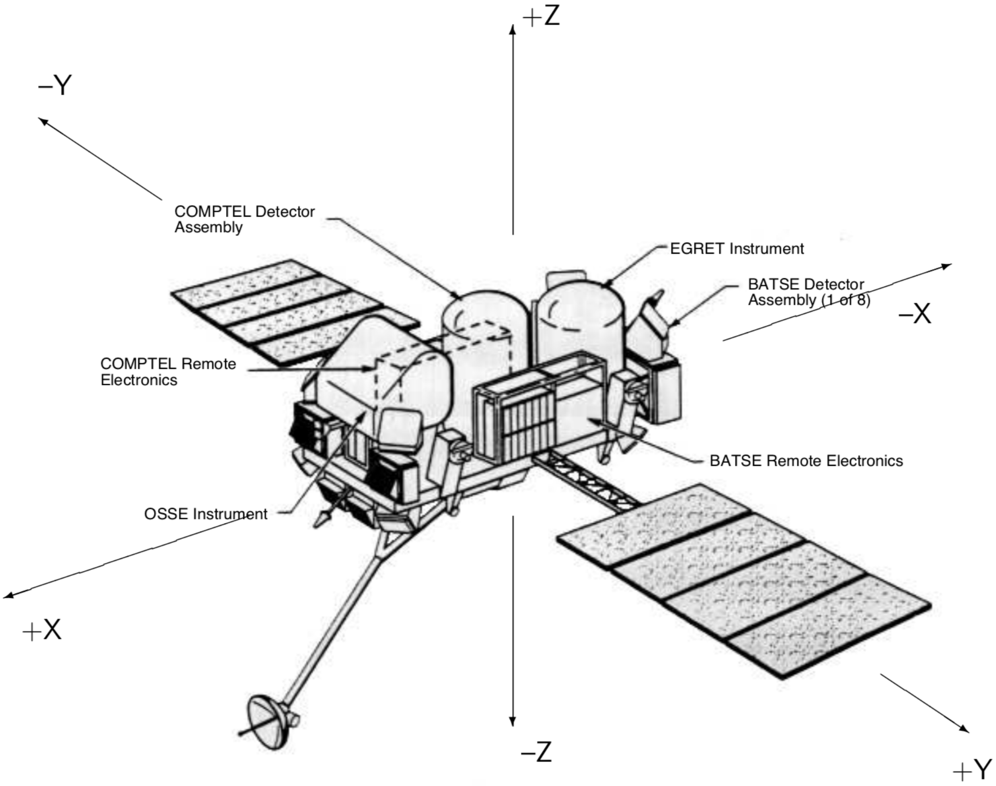

FIGURE 1.4: The Compton Gamma-Ray Observatory, with the positions of all detectors and instruments labeled as well as the positions of the x, y and z axes. Image adapted from Fishman et al., 1985.

Several studies have already attempted to estimate the unknown redshifts of GRBs based on the apparently-strong phenomenological correlations observed between some of the spectral and temporal prompt gamma-ray emission properties of GRBs. The most prominent class of such relations are the apparently-strong correlations of the intrinsic brightness measures of the prompt gamma-ray emission (e.g., the total isotropic emission, E_{iso}, and the peak 1024*ms* luminosity, L_{iso}) with other spectral or temporal properties of GRBs, such as *hardness* as measured by the intrinsic spectral peak energy E_{pz} (e.g., Yonetoku, Murakami, et al., 2004; Yonetoku, Nakamura, et al., 2014), light-curve variability (e.g., Fenimore and Ramirez-Ruiz, 2000; Daniel E Reichart et al., 2001), the spectral lag (e.g., B. E. Schaefer, Deng, and David L Band, 2001), or based on a combination of such relationships (e.g., Xiao and B. E. Schaefer, 2009; M. Dainotti et al., 2019).

These methods, however, can lead to incorrect or highly biased estimates of the unknown redshifts of GRBs if the observed high-energy correlations are constructed from a small sample of GRBs (typically the brightest events) with measured redshifts. Such small samples are often collected from multiple heterogeneous surveys and may neither represent the entire population of observed GRBs (with or without measured redshift) nor represent the unobserved cosmic population. More importantly, the potential effects of detector threshold and sample-incompleteness on them are poorly understood. Such biases manifest themselves in redshift estimates that are inconsistent with estimates from other methods, examples of which have been already reported by several authors (e.g., Cristiano Guidorzi, 2005; Ashcraft and B. E. Schaefer, 2007; Rizzuto et al., 2007; Bernardini et al., 2014).

The selection effects in the detection, analysis, and redshift measurements of GRBs and their potential effects on the observed phenomenological high-energy correlations have already been extensively studied individually, in isolation from other correlations, (e.g., Vahé Petrosian and T. T. Lee, 1996; Lloyd and Vahé Petrosian, 1999; Vahe' Petrosian, Lloyd-Ronning, and A. Lee, 1999; Lloyd, Vahé Petrosian, and Mallozzi, 2000; Hakkila et al., 2003; David L Band and Preece, 2005; Nakar and Piran, 2004; Nathaniel R Butler, Daniel Kocevski, Joshua S Bloom, and Curtis, 2007; Ghirlanda et al., 2008; Nava et al., 2008; Amir Shahmoradi and Robert Nemiroff, 2009; Nathaniel R Butler, Daniel Kocevski, and Joshua S Bloom, 2009; Nathaniel R Butler, Joshua S Bloom, and Poznanski, 2010; Amir Shahmoradi and Nemiroff, 2011; Shahmoradi and Nemiroff, 2011a; Amir Shahmoradi, 2013b; M. G. Dainotti et al., 2015; Vahé Petrosian, Kitanidis, and Daniel Kocevski, 2015). However, an ultimate resolution to the problem of estimating the unknown redshifts of GRBs in catalogs requires simultaneous multidimensional modeling of the intrinsic population distribution of GRB attributes, subject to the effects of detector threshold and sample incompleteness on their joint observed distribution (e.g., Nathaniel R Butler, Joshua S Bloom, and Poznanski, 2010; Amir Shahmoradi, 2013a; Amir Shahmoradi and Nemiroff, 2014; Amir Shahmoradi and Robert J Nemiroff, 2015).

Building upon the previous studies in the Computational Data Science Lab at the University of Texas at Arlington Amir Shahmoradi (2013b), Amir Shahmoradi (2013a), and Amir Shahmoradi and Robert J Nemiroff (2015), and motivated by the existing gap in the knowledge of the redshifts of GRBs in BATSE catalog (e.g., W. S. Paciesas et al., 1999; Goldstein et al., 2013), which as of 2020, constitutes the largest catalog of homogenously-detected GRBs, here we present a methodology and modeling approach to constraining the redshifts of 565 BATSE SGRBs. Despite lacking complete knowledge of the true cosmic rate and redshift distribution of SGRBs, we argue that it may be possible to constrain the redshifts of individual BATSE SGRBs (as well GRBs detected by other satellites) to within reasonable uncertainty ranges at high confidence levels.

The methodology presented in this work relies on two plausible assumptions which are strongly supported by the currently existing evidence: 1. SGRBs trace the cosmic Start Formation Rate (SFR) or a metallicity-corrected SFR (e.g., Nathaniel R Butler, Joshua S Bloom, and Poznanski, 2010; Pontzen et al., 2010), convolved with a binary merger delay-time distribution and, 2. the joint distribution of the four main prompt gamma-ray-emission properties of SGRBs is well described by a multivariate log-normal distribution (e.g., Amir Shahmoradi, 2013a; Amir Shahmoradi and Robert J Nemiroff, 2015). The presented work also paves the way toward a detector-independent minimally-biased phenomenological classification method for GRBs solely based on the intrinsic prompt gamma-ray data of individual events.

In the following sections, an attempt is presented to further uncover some of the tremendous amounts of useful, yet unexplored information that is still buried in this seemingly archaic catalog of GRBs. Towards this, we describe, in the following chapters, the development of a probabilistic redshift-inference methodology, including a discussion of the data collection procedure, a generic description of the probabilistic modeling approach via a toy problem, followed by detailed descriptions of the proposed methodology for estimating redshifts, the cosmic SFR assumptions underlying the proposed model for estimating the redshifts, the construction of an SGRB world model, and a review of the BATSE SGRB detection algorithm and the approach we use to model the BATSE SGRBs sample incompleteness. Finally, the predictions of the model are presented, followed by a discussion of the implications of the results.

Chapter 2

Data Collection

The *Burst and Transient Source Experiment* (BATSE) was a satellite that had a primary objective to study gamma-ray bursts, and functioned from April 1991- June 2000. It searched for GRBs and long-lived sources of GRBs. It was designed to trigger on changes of photon counts above a certain background level that was roughly 5.5 times the background photon count. The BATSE satellite was equipped with a four energy channel discriminator datatype known as DISCSC. Channel 1 had a range of 25-50 keV, channel 2 had a range of 50-100 keV, channel 3 had a range of 100-300 keV, and channel 4 had a range greater than 300 keV.

2.0.1 Gamma-ray detector instruments on BATSE satellite

There were eight detector modules on the BATSE satellite, each at one of the satellites corners. Each module consisted of two different NaI(Tl) scintillation detectors; a Large Area Detector (LAD) and a Spectroscopy Detector (SD). The LAD had a range of 20 KeV to 2 MeV, while the Spectroscopy Detector extended the upper energy range to 8 MeV.

Large Area Detectors

The primary detector of the BATSE satellite was the Large Area Detectors (LAD). A disc-shaped NAI(TI) crystal 1.27 cm thick and 50.8 cm in diameter, un-collimated for a large field of view, made up the LAD.

An optical window was created by mounting the crystal to a 1.91 cm layer of fused quartz and was attached to a light collection cone. Three 12.7 cm diameter photomultiplier tubes were coupled to the cone to collect the scintillation light. The outer layers of the collection cone were made of lead and tin, to act as a passive shield from gamma-rays coming from the back of the detector, and was effective up to 300-400 keV. The interior wall was coated with the highly reflective barium sulfate (BaSO4).

The charged-particle detector (CPD) was located in front of the LAD. The CPD was a 0.64 cm thick scintillator that was also used as a shield against charged particles. The scintillator was in the shape of an octagon with a width of 55.9 cm and was enclosed between two aluminum layers. Two 5.05 cm photomultiplier tubes attached to the plastic collected the scintillation light. The CPD and LAD worked in anti-coincidence mode and rejected events that were registered in both detectors. The energy threshold was approximately 500 KeV and the coincidence grating time was 2 μs (Gerald J Fishman, C. A. Meegan, et al., 1994).

The LAD had a higher sensitivity than the Spectroscopy Detectors (SD) due to its large detection area and offered a high energy resolution with a fine temporal resolution. To keep the 511 KeV electron annihilation line position in the detector's

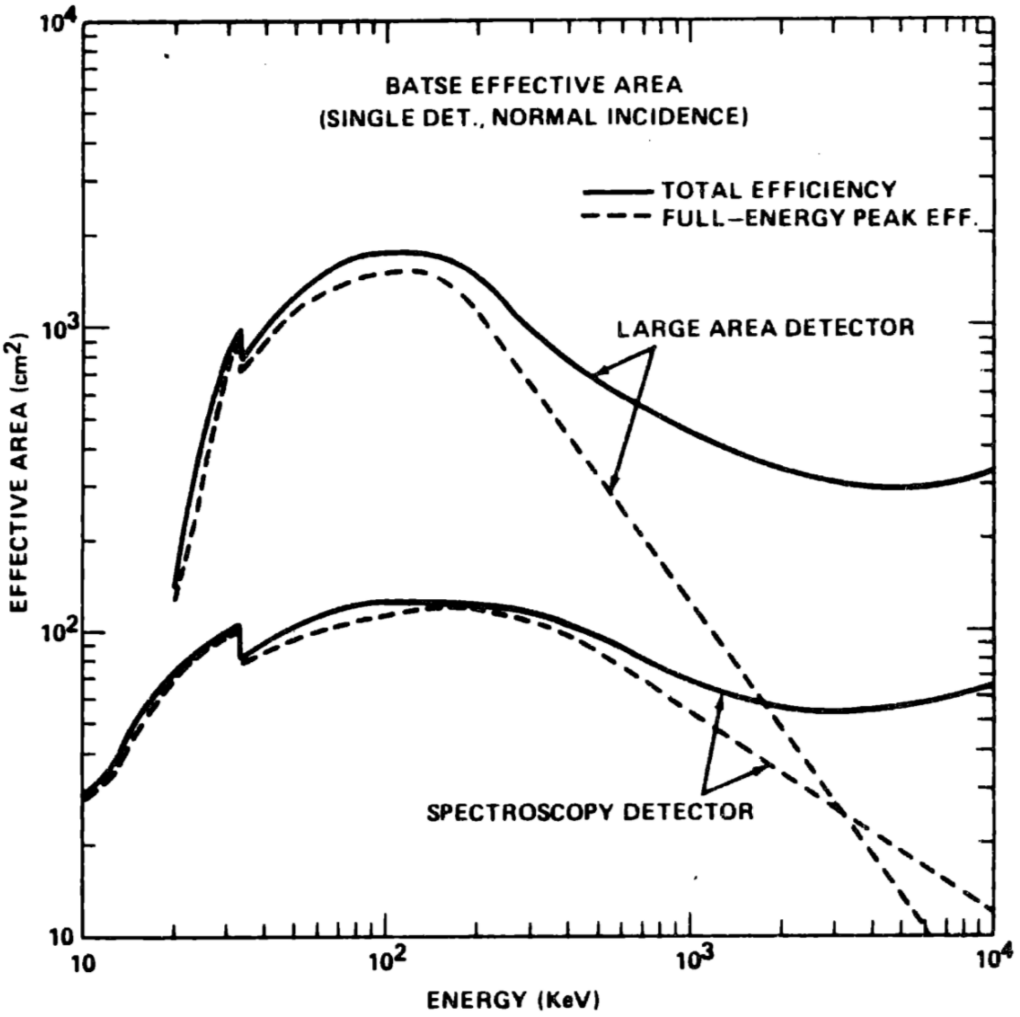

FIGURE 2.1: The effective detection energy windows of the BATSE satellite. Image adapted from Fishman et al., 1985.

TABLE 2.1: BATSE Instrument Characteristics

BATSE Instrument Characteristics	
Detectors	
Number of Detectors	Eight Large Area Detectors (LAD) Eight Spectroscopy Detectors (SD)
Field of View	Full Sky
Sensitive Area	2025 cm^2 per LAD 127 cm^2 per SD
Energy Range	20 KeV - 1.9 MeV for LAD 10 KeV - 100 MeV for SD
Experiment Sensitivities	
Burst Sensitivity	Eight Large Area Detectors (LAD) 3×10^{-8} ergs/cm^2 (1 sec burst)
Time Resolution	2 s minimum
Burst Location Accuracy	4.0 (strong burst)
Occulation Sensitivity (3)	100 mCrab (30-100 keV, one day)
FOB[1] Pulsed Source Sensitivity (3)	0.12 pulsed Crab (30-259 keV, typical day)
FOG[2] Pulsed Source Sensitivity (3)	0.05 pulsed Crab (30-250 keV, typical day)

[1] Folded-On-Board with special hardware
[2] Folded-On-Ground

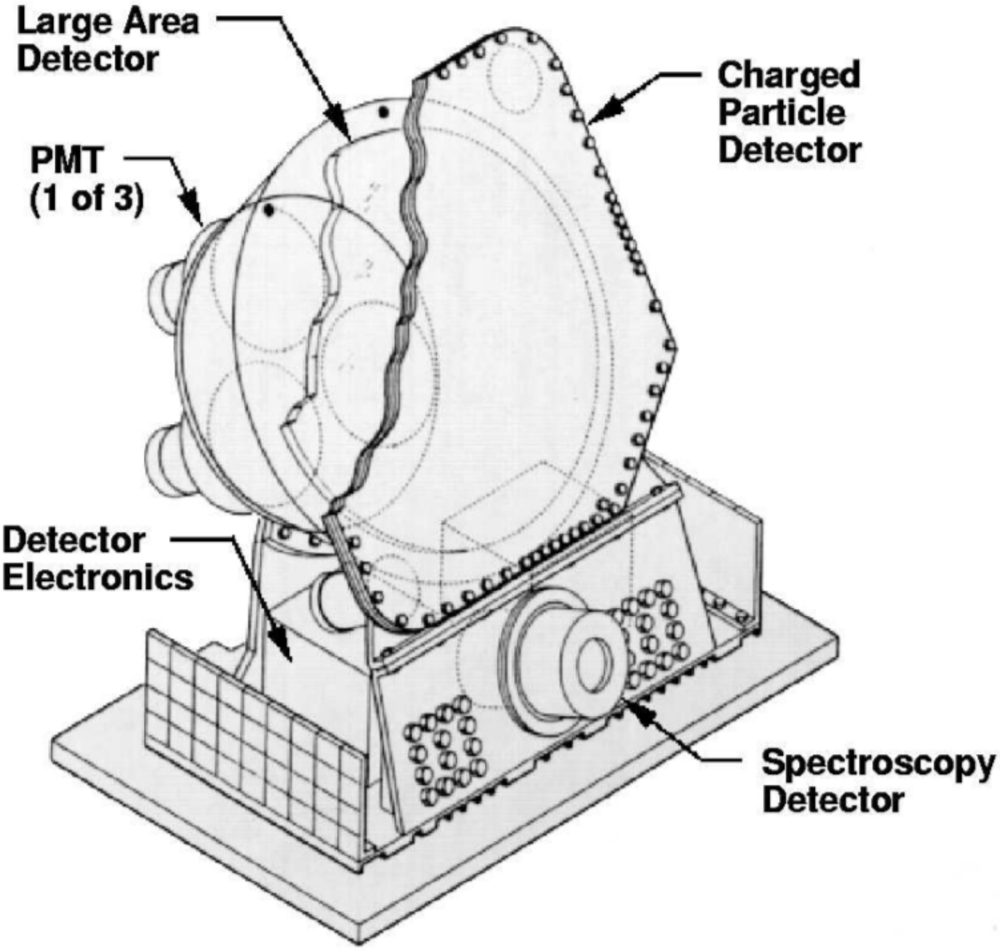

FIGURE 2.2: A BATSE detector module, containing both the LAD and the SD. Image adapted from Fishman et al., 1985.

channel space constant, the LAD used automatic gain control to stabilize the energy gain by adjusting the high voltage applied to the photomultiplier tubes. Each LAD had its energy range nearly fixed to 30 - 200 KeV during the mission.

Spectroscopy Detectors

The *Spectroscopy Detectors* (SDs) were also un-collimated NaI(TI) scintillation detectors, in the shape of a cylinder that was 7.62 cm thick with a 12.7 cm diameter. It was coupled directly to a photomultiplier tube, which was identical to the photomultiplier tubes used for the LADs. The tin and lead housing of the photomultiplier tube provided a passive shielding similar to the shielding used for the light collection cones of the LADs. The SD was mounted below the LAD on the BATSE module. The SD provided a much finer energy resolution then the LAD due to its geometry. A diagram of the SD is shown in 2.2. The gains of the SDs were commandable from the ground, unlike the LADs, which allowed broader energy coverage from as low as 5 KeV to as high as 20 MeV (Gerald J Fishman, C. A. Meegan, et al., 1994).

2.0.2 Statistical Properties of BATSE GRBs

The temporal and spatial occurrences of BATSE GRB events appear to be completely random, with each event's occurrence time and location in the sky completely independent of other events. As illustrated in Figure 2.3, the distribution of GRBs throughout the universe appears to be isotropic, and is not biased from one particular source but rather uniformly distributed in the sky. These observations provide strong evidence for cosmological origins of both classes of short and long duration GRBs.

Four main attributes are typically used to characterize the prompt gamma-ray emissions of gamma-ray bursts: the observed duration of the event (T_{90}), the frequency of energy release (bolometric fluence, S_{bol}), the peak brightness (bolometric peak flux P_{bol}), and the total energy received (observed peak energy, E_{p}). These are also known as the observed properties of a GRB, as seen from the reference frame of Earth. These observed properties are well illustrated in Figure 2.4.

The intrinsic properties of a GRB are these same properties measured with respect to the rest frame of a GRB, and are denoted as the rest-frame (intrinsic) duration (T_{90z}), the total isotropic emission (E_{iso}), the isotropic peak luminosity (L_{iso}), and the intrinsic spectral peak energy E_{pz}. Note that the use of the variable z in the subscripts is to indicate that the quantity is computed within the rest-frame of the event. With redshift (distance) information the intrinsic properties of a GRB are unknown to us. With the knowledge of redshift, however, they can be calculated using the following mapping equations:

$$L_{\mathrm{iso}} = 4\pi \times d_L(z)^2 \times P_{\mathrm{bol}} \tag{2.1}$$

$$E_{\mathrm{iso}} = 4\pi \times d_L(z)^2 \times S_{\mathrm{bol}}/(z+1) \tag{2.2}$$

$$E_{\mathrm{pz}} = E_{\mathrm{p}} \times (z+1) \tag{2.3}$$

$$T_{90\mathrm{z}} = T_{90}/(z+1)^{\alpha} \tag{2.4}$$

As seen in the equations above, there are also two other terms present: the cosmological luminosity distance ($d_L(z)$) and the redshift (z). The luminosity distance is dependent on the redshift and is given by (Amir Shahmoradi, 2013a)

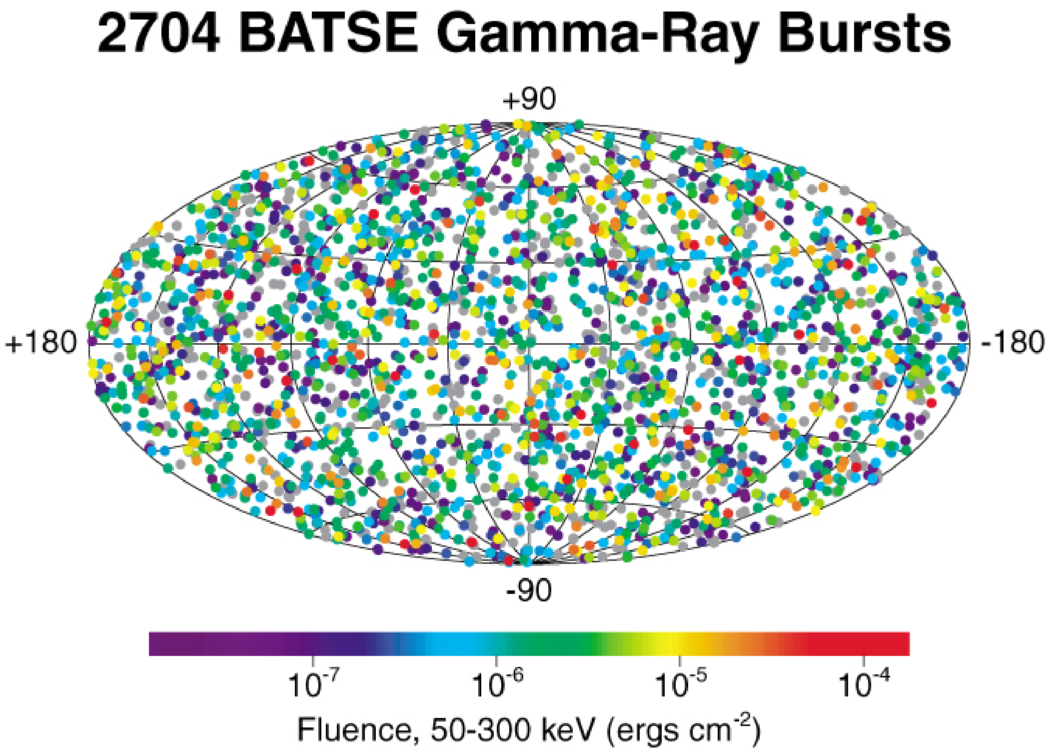

FIGURE 2.3: An illustration of the sky distribution of 2704 gamma-ray bursts detected by the BATSE instrument during nine years of observations. The bursts are isotropically distributed in the sky and located at cosmological distances far beyond the Milky Way Galaxy. Image credited to the NASA BATSE Team.

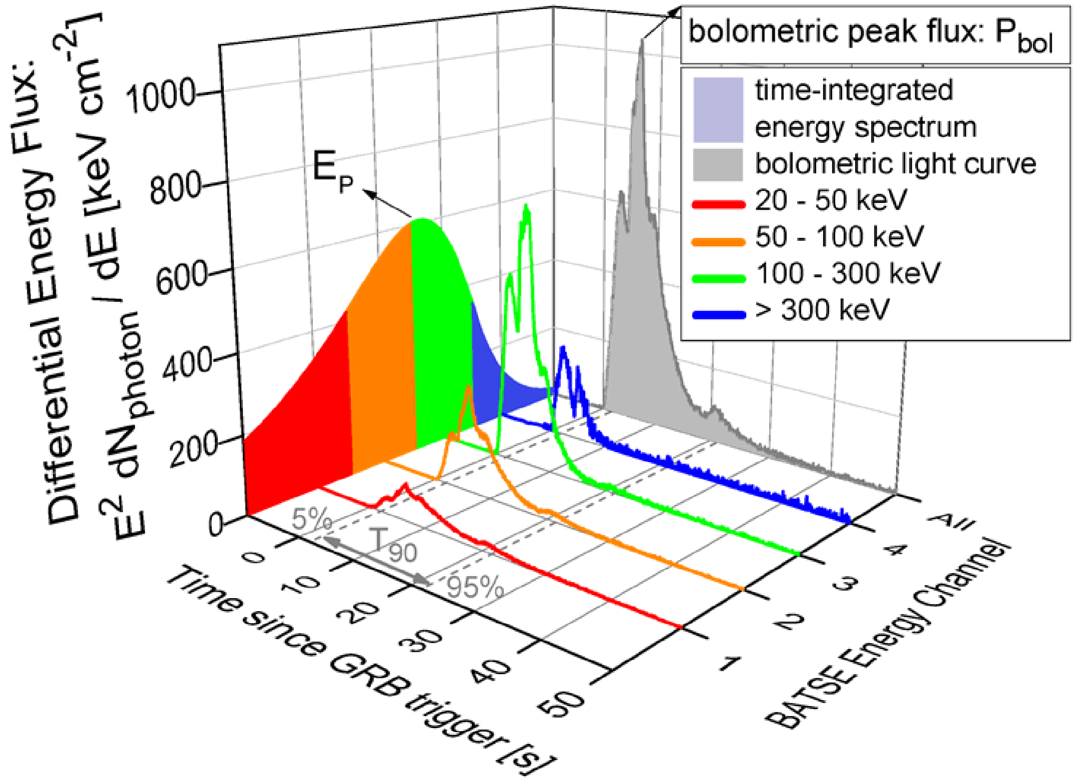

FIGURE 2.4: An illustration of the typical light-curve of a GRB. The x-axis represents the time since the GRB trigger was detected in seconds. The y-axis represents the differential energy flux, measured in KeV per cm^2. The z-axis represents the BATSE Energy Channel. For each GRB in our sample, we define a proxy measure of the spectral peak energy (E_p) by defining a spectral quantity known as the *Hardness Ratio*. The Hardness Ratio is computed by dividing the sum of total energy received in channels 3 and 4 to the sum of the energy received in channels 1 and 2 of the BATSE detectors. Amir Shahmoradi and Robert J Nemiroff, 2010 show that the Hardness Ratio is strongly and positively correlated with the spectral peak energies of BATSE GRBs.

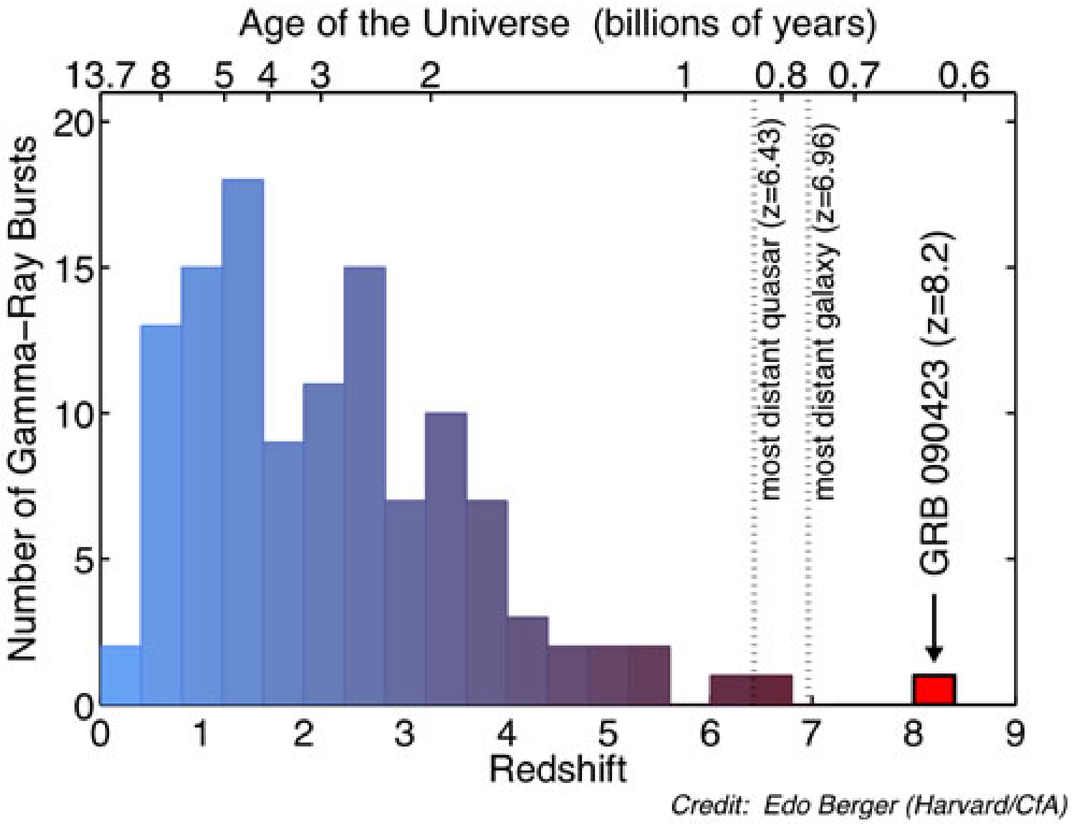

FIGURE 2.5: An illustration of the redshift distribution of GRBs as observed by the Fermi and Swift satellites. (Credits Berger, Harvard/CfA)

$$D_L(z) = \frac{C}{H_0}(1+z)\int_0^z dz' \left[(1+z')^3\Omega_M + \Omega_\Lambda\right]^{-1/2} \tag{2.5}$$

where C represents the speed of light, H_0 represents the Hubble constant, and Ω_M & Ω_Λ represent the Dark Matter and Dark Energy fractions in the universe, respectively. The cosmological parameters in 2.5 are set to $h = 0.70$, $\Omega_M = 0.27$, and $\Omega_\Lambda = 0.73$ (Jarosik et al., 2011).

Redshift Distribution

As mentioned before, the redshift distributions of BATSE GRBs are almost completely unknown. However, some studies (Amir Shahmoradi, 2013b; Amir Shahmoradi, 2014; Amir Shahmoradi and Robert J Nemiroff, 2015; Amir Shahmoradi and Robert J Nemiroff, 2015) indicate that the majority of BATSE GRBs originate from redshifts of 5 or less. Other more recent missions have had much more success in generating catalogs of GRBs with measured redshifts. For example, the distribution of the redshifts of SWIFT GRBs is shown in figure 2.5.

The spectral Peak Energies of BATSE GRBs

For many years, the BATSE catalog of GRBs only reported the basic properties of the prompt emissions of BATSE GRBs, most importantly, peak photon flux, the total energy received, and the observed T_{90} duration, defined as the interval within which 90% of the gamma-ray emission is received from the GRB event.

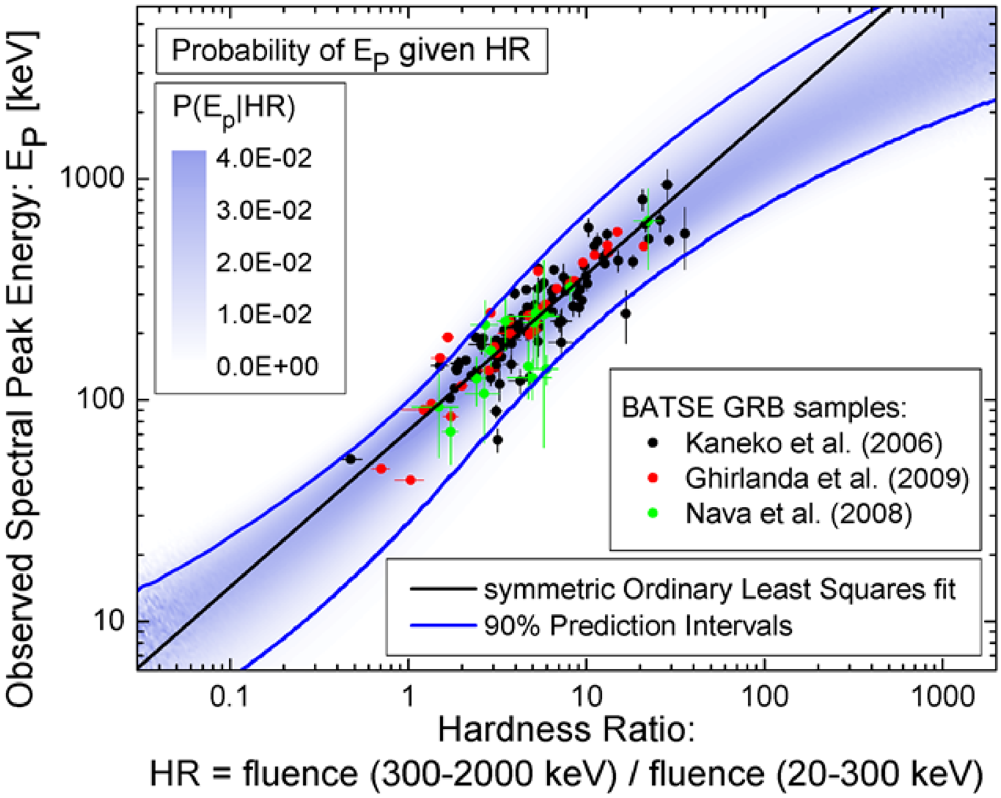

FIGURE 2.6: The relationship between the hardness ratio and the peak energy of BATSE GRB samples. All three models shown exhibit a strong correlation (as shown by the solid black line). The hardness ratio is used to calculate the peak energy, and using this attribute along with the other intrinsic values of GRBs the redshift can be calculated.

The spectral peak energies of BATSE GRBs however, have proven more difficult to compute, as their computation requires a careful analysis of the time-integrated spectra of events. In response to the need for knowing the peak energies of BATSE GRBs, Amir Shahmoradi and Robert J Nemiroff, 2010; Shahmoradi and Nemiroff, 2011b discovered and quantified a tight relationship between an easily measured quantity from the BATSE catalog and the known spectral peak energies of a limited sample of bright BATSE GRBs (Figure 2.6). This quantity, named the *Hardness Ratio* (HR), is the ratio of the sum of the total energy received (i.e., energy fluence) in channels 4 and 3 of the BATSE LAD detectors to the sum of the energy fluence received in channels 2 and 1 of the BATSE LADs (Amir Shahmoradi and Robert J Nemiroff, 2010). Channels 3 and 4 of the BATSE LAD detectors measured within the energy range of 300-2000 keV, while channels 1 and 2 measured within the 20-300 KeV energy range.

Using this proxy measure, Amir Shahmoradi and Robert J Nemiroff, 2010 were able, for the first time, to estimate the observed spectral peak energies of >2130 BATSE GRBs, and reconstruct the distribution of the BATSE spectral peak energies as illustrated in Figure 2.7.

The knowledge of the peak energies together with duration measurements then enabled Amir Shahmoradi, 2013b; Amir Shahmoradi, 2013a; Amir Shahmoradi, 2014;

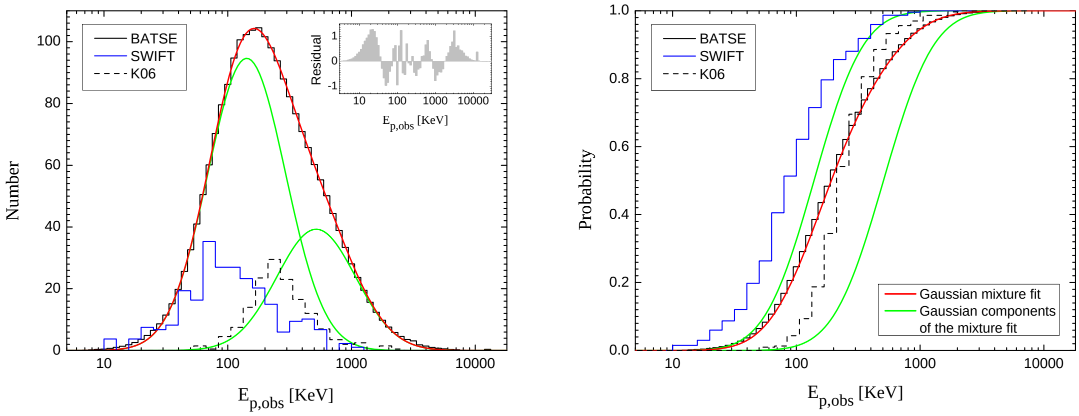

FIGURE 2.7: Left: The probability distribution function of the observed peak energy ($E_{\mathrm{p,obs}}$). The black solid line is the distribution of 2130 BATSE GRBs $E_{\mathrm{p,obs}}$, and the small inserted graph represents the residuals of the fit. The two green lines are the mixture decomposition of the BATSE catalog $E_{\mathrm{p,obs}}$ into two Gaussians. The two Gaussians could represent the $E_{\mathrm{p,obs}}$ of BATSE LGRBs (peaking at 140 KeV) and the $E_{\mathrm{p,obs}}$ of BATSE SGRBs (peaking at 520 KeV). Figures adapted from Amir Shahmoradi and Robert J Nemiroff, 2010

Amir Shahmoradi and Robert J Nemiroff, 2015 to perform a minimally-biased homogeneous fuzzy (probabilistic) classification of BATSE GRBs into the two major classes of short and long GRBs. The resulting two classes are illustrated in Figure 2.8

The distributions of four main observational properties of BATSE GRBs for the two classes of short and long durations are illustrated in Figure 2.9.

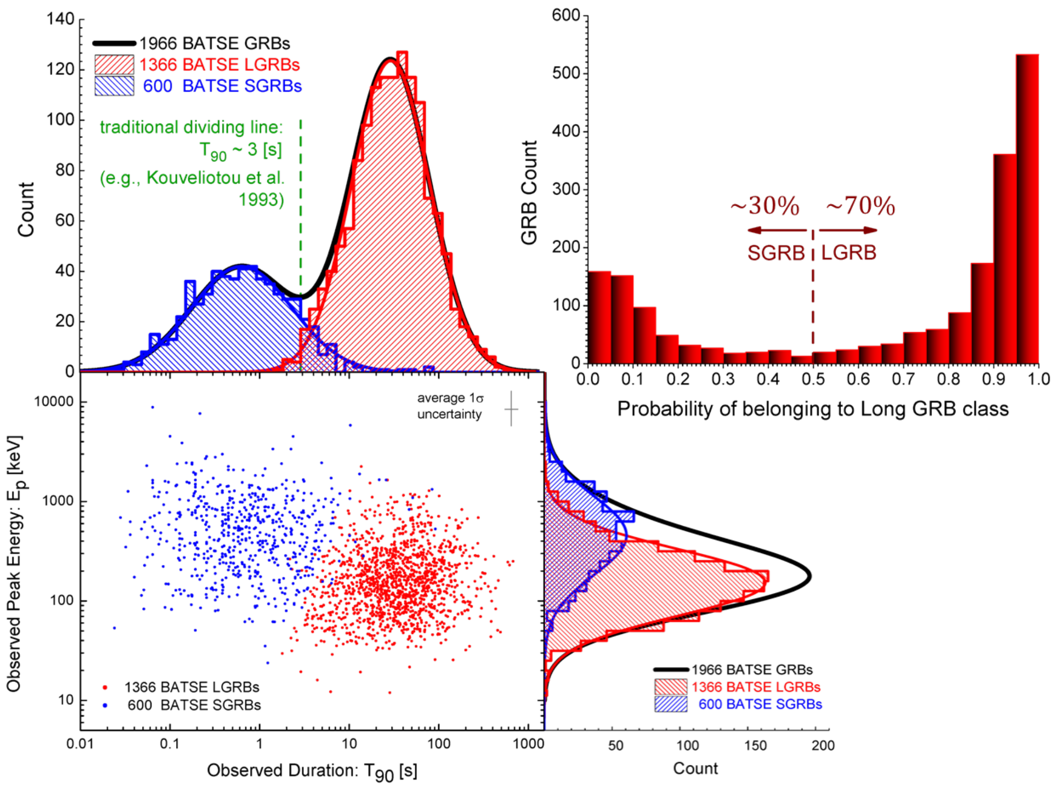

FIGURE 2.8: The classification of 1966 BATSE GRBs into short and long gamma-ray bursts. The observed duration (T_{90}), measured peak flux (P_{bol}), and fluence (S_{bol}) are taken from the current BATSE catalogue. The measured spectral peak energies are taken from Amir Shahmoradi and Robert J Nemiroff, 2010. A fuzzy C-means clustering algorithm using the T_{90} and E_{p} GRB variables was used to separate the subcategories of GRBs. Figure adapted from Amir Shahmoradi and Robert J Nemiroff, 2015.

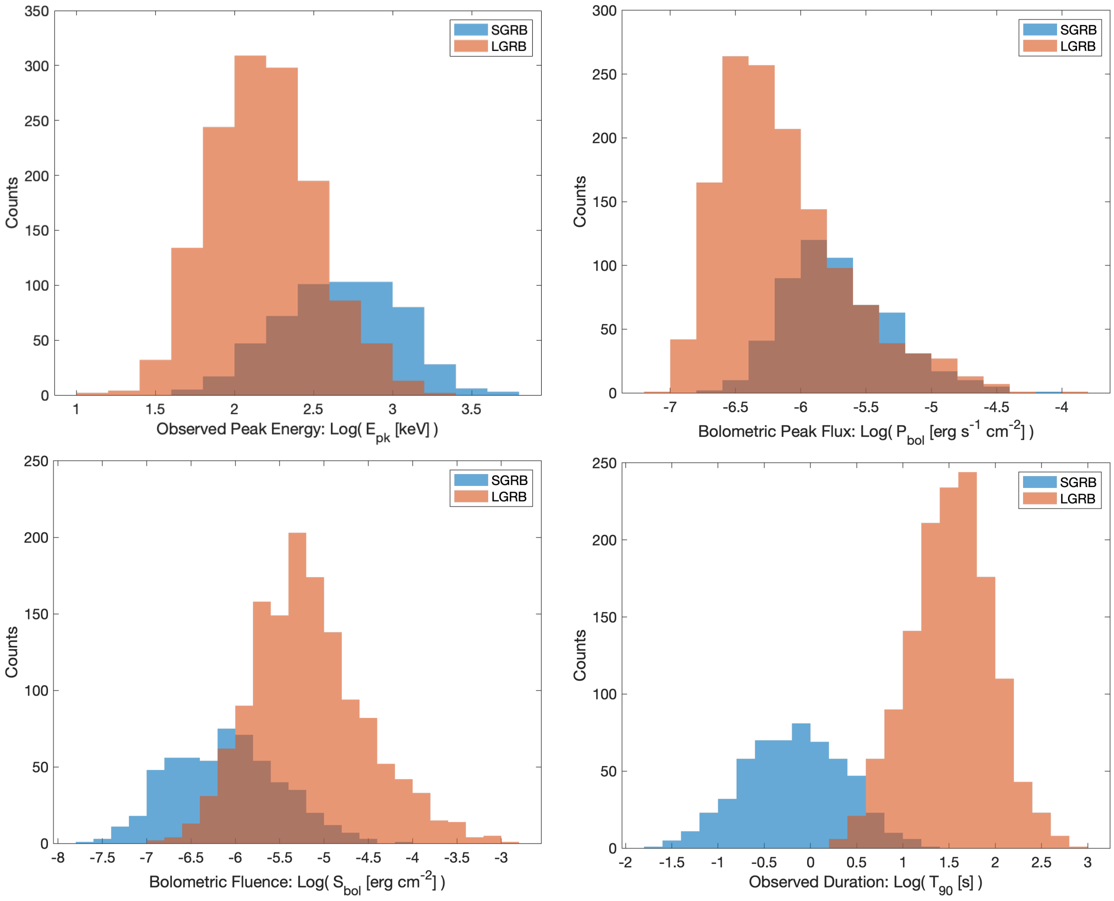

FIGURE 2.9: Histograms showing how the distributions of the four main attributes of gamma-ray bursts compare between long and short bursts.

Chapter 3

Methodology

3.1 The Need for Bayesian Probability Theory

As stated back in section 2.0.2 we have four equations that relate the intrinsic properties to the quantities we have observed. The problem, however, is that we have two unknowns in each equation; the unknowns being the intrinsic properties and redshift. Algebraically we cannot solve this. However, as we show in this body of work, we can still use the principles of the Bayesian probability theory to solve this problem.

In the following sections, I explain some of the foundations of Bayesian probability theory that are required for the subsequent analysis presented in this work.

3.2 Foundation of Bayesian Probability Theory

A careful look at the history of Probability Theory reveals that there have been three major definitions for probability. The Classical probability theory that began in the 18th century, defines probability as the degree of belief that an outcome will occur, and allows for prior knowledge to be used in the inference. Around the beginning of the 19th century, an alternative definition of probability known as the Frequentist probability emerges which defines probability as the relative frequency of occurrence of an outcome. This new paradigm does not allow for prior knowledge to be used in the inference.

At the beginning of the 20th century a new movement, in particular, from within the fields of Physics and Economics, led to the resurgence of the classical definition of the probability theory, with the foundations and formalism of the theory being more rigorously than before. This notion of Probability has now become known as *Bayesian Probability Theory*.

3.2.1 A simple intuitive proof of the Bayes' Rule

The entire Bayesian Probability Theory revolves around a fundamental equation known as the Bayes' rule. A vigorous proof of Bayes's theorem is beyond the scope of this dissertation. Here I only present a simplified proof of the Bayes theorem via Venn diagrams.

Suppose our entire universe is represented by a circle labeled 'universe', as shown in figure 3.1. Within this circle, we are interested in the probability of us living in the circle A. That probability is computed via this equation, represented as $P(A)$, and is defined as the area of A divided by the area of the universe U, represented as $P(A) = A/U$. Similarly, if there is another circle B, the probability of us living in B is given as $P(B) = B/U$.

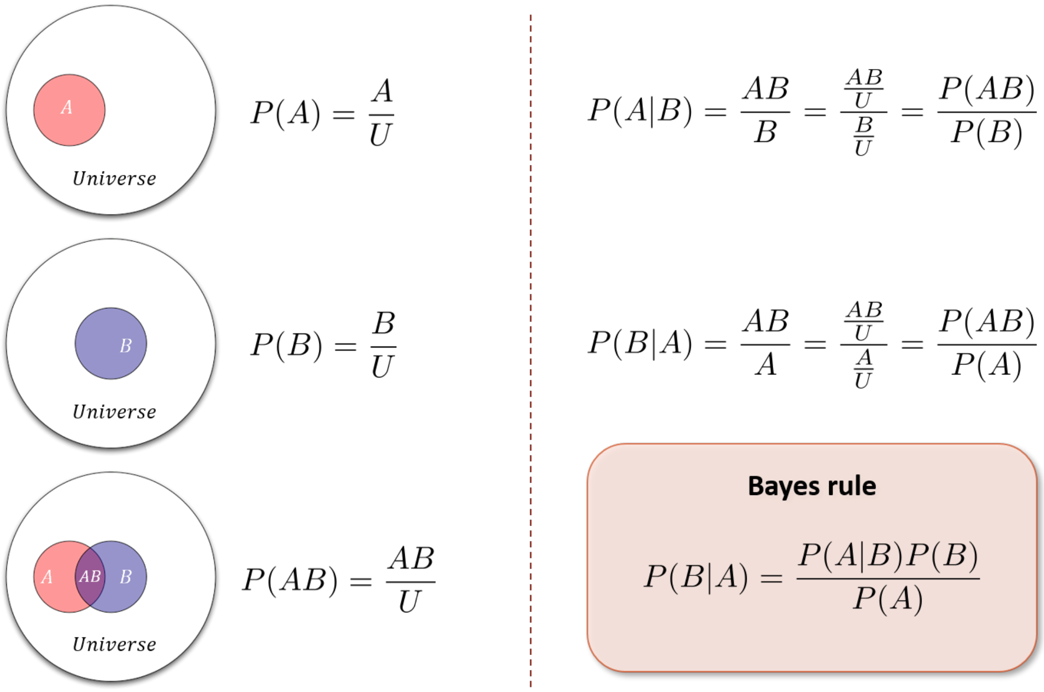

FIGURE 3.1: The proof of the Bayes Rule via Venn diagrams.

Now consider the case where both A and B overlap each other, created a joint space AB. Then the probability of living in this joint space is the area of the overlap section divided by the area of the universe, or $P(AB) = AB/U$.

Continuing further, what if we knew that we were in the circle B, and wanted to know the probability of being in circle A? This probability is represented as $P(A|B)$, or 'the probability of A given B. To find this probability you would simply divide the area of the overlap AB by the area of B. By dividing each term in the fraction by the area of the universe U it can be shown that this is the same as the probability $P(AB)$ divided by $P(B)$.

$$P(A|B) = \frac{AB}{B} = \frac{AB/U}{B/U} = \frac{P(AB)}{P(B)}$$

Similarly, if we knew that we were in the area A and wanted to find the probability that we were also in B, that would be given by

$$P(B|A) = \frac{AB}{A} = \frac{AB/U}{A/U} = \frac{P(AB)}{P(A)}$$

We can then rewrite this as

$$P(B|A) = \frac{P(AB)}{P(A)} = \left(\frac{P(AB)}{P(B)}\right)\frac{P(B)}{P(A)} = \frac{P(A|B)P(B)}{P(A)}$$

This is Bayes rule, which tells us that 'the probability of B given A is equal to the probability of A given B times the probability of B divided by the probability of A.'

By convention unobservable parameters are represented by Greek letters in this work. Observable quantities are represented by English letters and mathematical sets are represented by script letters. Using this convention, the Bayes rule for a

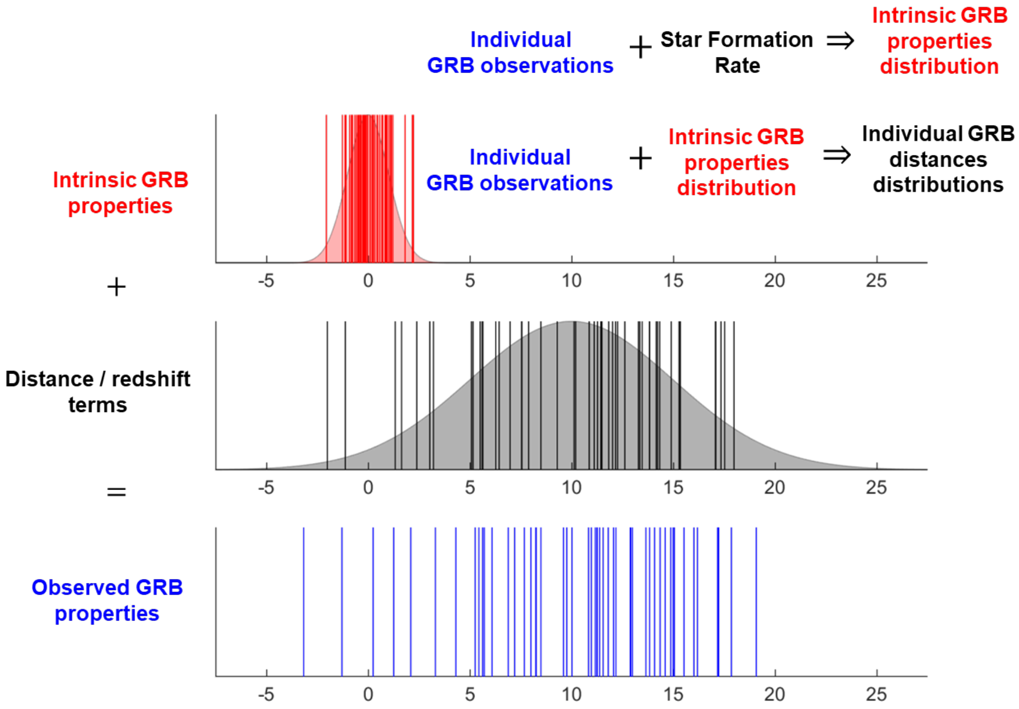

FIGURE 3.2: In this figure the methodology used to infer the redshifts of BATSE GRBs is shown. The red lines represent a distribution of the unknown intrinsic properties of a GRB, while the blue lines represent a distribution of the known observed properties of a GRB, and the black lines represent a distribution of the unknown redshift of the GRB.

mathematical modeling problem can be written as,

$$\pi\left(\boldsymbol{\theta}|\mathcal{D},M\right) = \frac{\pi\left(\mathcal{D}|\boldsymbol{\theta},M\right)\pi\left(\boldsymbol{\theta}|M\right)}{\pi\left(\mathcal{D}|M\right)} \tag{3.1}$$

where probability is represented by $\pi(\cdot)$, while our data set is represented by $\mathcal{D}$, our model is represented by M, and the parameters of the model are represented by $\boldsymbol{\theta}$. The term $\pi\left(\boldsymbol{\theta}|\mathcal{D},M\right)$ represents the posterior distribution of the parameters given the model and the observational data, $\pi\left(\mathcal{D}|\boldsymbol{\theta},M\right)$ is the likelihood function, $\pi\left(\boldsymbol{\theta}|M\right)$ is the prior distribution representing our prior knowledge about the parameters of the model, and $\pi\left(\mathcal{D}|\boldsymbol{\theta},M\right)$ is a normalization constant, known as the evidence.

To understand the logic of the Multilevel Empirical Bayesian modeling, which underlies this work, consider the following problem outlined in the section below.

3.2.2 An Illustration of the Methodology with a Toy Problem

Consider two distributions, one representing the intrinsic GRB properties and one representing the redshift terms of the GRBs. By convolving these two distributions the observed GRB distribution can be calculated.

Without loss of generality, suppose the observed properties of individual BATSE SGRBs are exactly known, with no measurement error, as illustrated by the individual blue-colored vertical lines in the bottom plot of Figure 3.2. The corresponding redshifts of these events, (represented by the black lines in the middle plot of Figure 3.2) are, however, unknown and we wish to estimate them. Although we have no knowledge of the joint population distribution of the intrinsic properties of SGRBs, illustrated by the red distribution in the top plot of Figure 3.2, there are strong arguments in favor of these properties being potentially well-described by a 4-dimensional multivariate log-normal distribution, $\mathcal{N}(\boldsymbol{\mu}, \boldsymbol{\Sigma})$ in the space of $L_{\rm iso}$, $E_{\rm iso}$, $E_{\rm pz}$, and $T_{\rm 90z}$ (Amir Shahmoradi, 2013a; Amir Shahmoradi and Robert J Nemiroff, 2015). Here, $\boldsymbol{\mu}$ and $\boldsymbol{\Sigma}$ represent the mean and the covariance matrix of the multivariate log-normal distribution, respectively.

We now reach the crucial step in the inference process: Despite the complete lack of information about the redshifts of BATSE SGRBs, we can use the existing prior knowledge about the overall cosmic redshift distribution of SGRBs to integrate over all possible redshifts for each observed SGRB in BATSE catalog to infer a range of plausible values for the intrinsic properties of the corresponding SGRB. These individually-computed probability density functions (PDFs) of the intrinsic properties can be then used to infer the unknown parameters $(\boldsymbol{\mu}, \boldsymbol{\Sigma})$ of the joint population distribution of the intrinsic properties of SGRBs (i.e., the multivariate log-normal distribution).

Once the parameters $(\boldsymbol{\mu}, \boldsymbol{\Sigma})$ are constrained, we can use the inferred population distribution of the intrinsic SGRB properties together with the observed properties to estimate the redshifts of individual BATSE SGRBs, independently of each other. The estimated redshifts can be again used to further constrain $\mathcal{N}(\boldsymbol{\mu}, \boldsymbol{\Sigma})$ which will then result in even tighter estimates for the individual redshifts of BATSE SGRBs. This recursive progress can practically continue until convergence to a set of fixed individual redshift estimates occurs.

At first glance, this simple semi-Bayesian mathematical approach may sound like magic and perhaps, too good to be true. Sometimes it is. However, as explained in the following sections, it can also lead to reasonably-accurate results if some conditions regarding the problem and the observational dataset are satisfied.

3.3 Estimating the Unknown Redshifts of BATSE SGRBs

The lack of knowledge of the cosmic rate of SGRBs proves to be the largest source of uncertainty when doing population studies. Very few redshifts are known, and these are typically limited to the brightest events. However, as stated in the previous section these limitations can be mitigated to some extent by the Bayesian Probability Theory. In this section a more formal presentation of the Empirical multilevel Bayesian methodology is provided. First, a probabilistic approach to estimating the cosmic rates of SGRBs is presented. Then we use the constrained cosmic rates model to infer the unknown redshifts of BATSE SGRBs.

3.3.1 Constraining the Cosmic Rates of Occurrence of SGRBs

Let $\boldsymbol{D}^{\rm g}_{\rm obs,i}$, represent the ith SGRB event, with the four main GRB prompt emission properties,

$$\boldsymbol{D}^{\rm g}_{\rm obs,i} = \left[P_{\rm bol,i}, S_{\rm bol,i}, E_{\rm p,i}, T_{\rm 90,i}\right] . \tag{3.2}$$

These are essentially the values reported both in the BATSE catalog and in Amir Shahmoradi and Robert J Nemiroff (2010).

The entire BATSE dataset of 565 SGRB events attributes can then be represented as the collection of these events,

$$\mathcal{D}^{\rm g}_{\rm obs} = \left\{\boldsymbol{D}^{\rm g}_{\rm obs,i} : 1 \leq i \leq 565\right\} \tag{3.3}$$

The peak brightness, $P_{\rm bol}$, is included in our GRB world model as it, along with $E_{\rm p}$, determines the peak photon flux, $P_{\rm ph}$, in the $50-300$ [keV] range.

Given the available observed BATSE dataset, $\mathcal{D}^{\rm g}_{\rm obs}$, the primary goal in estimating the redshift values is to constrain the probability density functions of the redshifts of individual BATSE SGRBs. To do this, the process of SGRB observation is modeled as a non-homogeneous Poisson process whose mean rate parameter is the 'observed' cosmic SGRB rate, $\mathcal{R}_{cen}$.

Each SGRB can be described as having the intrinsic properties,

$$\boldsymbol{D}^{\rm g}_{\rm int,i} = [L_{\rm iso,i}, E_{\rm iso,i}, E_{\rm pz,i}, T_{\rm 90z,i}] \tag{3.4}$$

$$\boldsymbol{D}_{\rm int,i} = \{\boldsymbol{D}^{\rm g}_{\rm int,i}, z_i :\ 1 \leq i \leq 565\} \tag{3.5}$$

in the 5-dimensional attributes space, $\Omega(\boldsymbol{D}_{\rm int})$, of the 1024 [ms] isotropic peak luminosity ($L_{\rm iso}$), the total isotropic emission ($E_{\rm iso}$), the intrinsic spectral peak energy ($E_{\rm pz}$), and the intrinsic duration ($T_{\rm 90z}$), as a function of the parameters, $\boldsymbol{\theta}_{\rm obs}$, of the observed SGRB rate model, $\mathcal{R}_{cen}$. The probability of these SGRBs occurring with the given properties is then given by,

$$\pi\left(\boldsymbol{D}_{\rm int,i}|\mathcal{R}_{cen}, \boldsymbol{\theta}_{\rm obs}\right) \propto \mathcal{R}_{cen}\left(\boldsymbol{D}_{\rm int,i}, \boldsymbol{\theta}_{\rm obs}\right) \tag{3.6}$$

where the term $\mathcal{R}_{cen}$ represents the BATSE-censored rate of SGRB occurrence in the universe. This can also be rewritten in terms of the intrinsic cosmic SGRB rate, $\mathcal{R}_{tru}$, along with the BATSE detection efficiency function, $\eta_{\rm eff}$, as

$$\begin{aligned} \frac{{\rm d}N_{\rm obs}}{{\rm d}\boldsymbol{D}_{\rm int}} &= \mathcal{R}_{cen}\left(\boldsymbol{D}_{\rm int}, \boldsymbol{\theta}_{\rm obs}\right) , \\ &= \eta_{\rm eff}\left(\boldsymbol{D}_{\rm int}, \boldsymbol{\theta}_{\rm eff}\right) \times \mathcal{R}_{tru}\left(\boldsymbol{D}_{\rm int}, \boldsymbol{\theta}_{\rm int}\right) , \end{aligned} \tag{3.7}$$

for a given set of input intrinsic SGRB attributes, $\boldsymbol{D}_{\rm int}$, with $\boldsymbol{\theta}_{\rm obs} = \{\boldsymbol{\theta}_{\rm eff}, \boldsymbol{\theta}_{\rm int}\}$ as the set of the parameters of our models for the BATSE detection efficiency and the intrinsic cosmic SGRB rate, respectively. Assuming that there is no systematic evolution of SGRB characteristics with the redshift, the intrinsic SGRB rate itself can be written as,

$$\begin{aligned} \frac{{\rm d}N_{\rm int}}{{\rm d}\boldsymbol{D}_{\rm int}} &= \mathcal{R}_{tru}\left(\boldsymbol{D}_{\rm int}, \boldsymbol{\theta}_{\rm int}\right) \\ &= \mathcal{R}^{\rm g}_{tru}\left(\boldsymbol{D}^{\rm g}_{\rm int}, \boldsymbol{\theta}^{\rm g}_{tru}\right) \times \frac{\dot{\zeta}(z, \boldsymbol{\theta}_z){\rm d}V/{\rm d}z}{(1+z)} , \end{aligned} \tag{3.8}$$

with $\boldsymbol{\theta}_{\rm int} = \{\boldsymbol{\theta}^{\rm g}_{tru}, \boldsymbol{\theta}_z\}$, where $\mathcal{R}^{\rm g}_{tru}$ is a statistical model, with $\boldsymbol{\theta}^{\rm g}_{tru}$ denoting its parameters, that describes the population distribution of SGRBs in the 4-dimensional attributes space of $\boldsymbol{D}^{\rm g}_{\rm int} = [L_{\rm iso}, E_{\rm iso}, E_{\rm pz}, T_{\rm 90z}]$, and the term $\dot{\zeta}(z, \boldsymbol{\theta}_z)$ represents the comoving rate density model of SGRBs with the set of parameters $\boldsymbol{\theta}_z$, while the factor $(1+z)$ in the denominator accounts for the cosmological time dilation. The comoving volume element per unit redshift, ${\rm d}V/{\rm d}z$, is given by (e.g., Winberg, 1972; Peebles, 1993),

$$\frac{{\rm d}V}{{\rm d}z} = \frac{C}{H_0} \frac{4\pi {d_L}^2(z)}{(1+z)^2\left[\Omega_M(1+z)^3 + \Omega_\Lambda\right]^{1/2}} , \tag{3.9}$$

with d_L standing for the luminosity distance as given in (3.9). If the three rate models, $(\dot{\zeta}, \eta_{\mathrm{eff}}, \mathcal{R}^{\mathrm{g}}_{tru})$, and their parameters were known a priori, one could readily compute the PDFs of the set of unknown redshifts of all BATSE SGRBs,

$$\mathcal{Z} = \left\{ z_i : 1 \leq i \leq 565 \right\} , \tag{3.10}$$

as,

$$\pi\left(\mathcal{Z} | \mathcal{D}^{\mathrm{g}}_{\mathrm{obs}}, \mathcal{R}_{cen}, \boldsymbol{\theta}_{\mathrm{obs}}\right) \propto \mathcal{R}_{cen}\left(\mathcal{Z}, \mathcal{D}^{\mathrm{g}}_{\mathrm{obs}}, \boldsymbol{\theta}_{\mathrm{obs}}\right) . \tag{3.11}$$

For a range of possible parameter values, the redshift probabilities can be computed by marginalizing over the entire parameter space, $\Omega(\boldsymbol{\theta}_{\mathrm{obs}})$, of the model,

$$\begin{aligned} \pi\left(\mathcal{Z}\right. & \left| \quad \mathcal{D}^{\mathrm{g}}_{\mathrm{obs}}, \mathcal{R}_{cen}\right) \\ = & \int_{\Omega(\boldsymbol{\theta}_{\mathrm{obs}})} \pi\left(\mathcal{Z} | \mathcal{D}^{\mathrm{g}}_{\mathrm{obs}}, \mathcal{R}_{cen}, \boldsymbol{\theta}_{\mathrm{obs}}\right) \\ \times & \quad \pi\left(\boldsymbol{\theta}_{\mathrm{obs}} | \mathcal{D}^{\mathrm{g}}_{\mathrm{obs}}, \mathcal{R}_{cen}\right) \mathrm{d}\boldsymbol{\theta}_{\mathrm{obs}} . \end{aligned} \tag{3.12}$$

The problem, however, is that neither the rate models nor their parameters are known a priori. Even more problematic is the circular dependency of the posterior PDFs of $\mathcal{Z}$ and $\boldsymbol{\theta}_{\mathrm{obs}}$ on each other,

$$\begin{aligned} \pi\left(\boldsymbol{\theta}_{\mathrm{obs}}\right. & \left| \quad \mathcal{D}^{\mathrm{g}}_{\mathrm{obs}}, \mathcal{R}_{cen}\right) \\ = & \int_{\Omega(\mathcal{Z})} \pi\left(\boldsymbol{\theta}_{\mathrm{obs}} | \mathcal{Z}, \mathcal{D}^{\mathrm{g}}_{\mathrm{obs}}, \mathcal{R}_{cen}\right) \\ \times & \quad \pi\left(\mathcal{Z} | \mathcal{D}^{\mathrm{g}}_{\mathrm{obs}}, \mathcal{R}_{cen}\right) \mathrm{d}\mathcal{Z} . \end{aligned} \tag{3.13}$$

Therefore, we adopt the following methodology, which is reminiscent of the Empirical Bayes (Robbins, 1985) and Expectation-Maximization algorithms (Dempster, Laird, and Rubin, 1977), to estimate the redshifts of BATSE SGRBs. First, we propose models for $(\dot{\zeta}, \eta_{\mathrm{eff}}, \mathcal{R}^{\mathrm{g}}_{tru})$, whose parameters have yet to be constrained by observational data. Given the three rate models, we can then proceed to constrain the free parameters of the observed cosmic SGRB rate, $\mathcal{R}_{cen}$, based on BATSE SGRB data.

The most appropriate fitting approach should take into account the observational uncertainties and any prior knowledge from independent sources. This can be achieved via the multilevel Bayesian methodology (e.g., Amir Shahmoradi, 2017) by constructing the likelihood function and the posterior PDF of the parameters of the model, while taking into account the uncertainties in observational data (e.g., Eqn. 61 in Amir Shahmoradi, 2017; Amir Shahmoradi and Robert J Nemiroff, 2019),

$$\begin{aligned} & \pi\left(\boldsymbol{\theta}_{\mathrm{obs}} | \mathcal{D}^{\mathrm{g}}_{\mathrm{obs}}, \mathcal{R}_{cen}\right) \\ = & \exp\left(- \int_{\Omega(\boldsymbol{D}_{\mathrm{int}})} \mathcal{R}_{cen}\left(\boldsymbol{D}^{*}_{\mathrm{int}}, \boldsymbol{\theta}_{\mathrm{obs}}\right) \mathrm{d}\boldsymbol{D}^{*}_{\mathrm{int}} \right) \\ \times & \prod_{i=1}^{565} \eta_{\mathrm{eff}}\left(\boldsymbol{D}^{\mathrm{g}}_{\mathrm{obs,i}}, \boldsymbol{\theta}_{\mathrm{eff}}\right) \int_{z^{*}=0}^{z^{*}=+\infty} \mathcal{R}_{tru}\left(\boldsymbol{D}^{\mathrm{g}}_{\mathrm{obs,i}}, z^{*}, \boldsymbol{\theta}_{\mathrm{int}}\right) \mathrm{d}z^{*}, \end{aligned} \tag{3.14}$$

where (3.14) holds under the assumptions of independent and identical distribution (i.e., the i.i.d. property) of BATSE SGRBs, and no measurement uncertainty in the observational data, except redshift (z) which is completely unknown for BATSE SGRBs.

Once the posterior PDF of the model parameters is obtained, it can be plugged into (3.12) to constrain the redshift PDF of individual BATSE SGRBs at the second level of modeling.

3.3.2 The SGRB Redshift Prior Knowledge

The main assumption in this work is that SGRBs are due to the coalescence of binary Neutron stars or the merger of a Neutron star and a black hole. It is widely believed that the binary mergers require significant cosmological time to occur after the deaths of the parent stars and the formations of the Neutron stars. In this scenario, the cosmic rate of SGRBs follows the Star Formation Rate (SFR) convolved with a distribution of the *delay time* between the formation of a binary system and its coalescence due to gravitational radiation.

There is currently no consensus on the statistical moments and shape of the distribution of the delay time between the deaths of supermassive stars and their subsequent coalescence to form SGRBs, solely based on observations of individual events and their host galaxies. The median delays vary widely in the range of $\sim 0.1-7$ billion years depending on the assumptions involved in estimation methods or in the dominant binary formation channels considered. Recent results from population synthesis simulations however, favor very short delay times of a few hundred million years with a long negligible tail towards several billion years (e.g., Amir Shahmoradi and Robert J Nemiroff, 2015).

The computational expenses and limitations imposed on this work strongly limit the number of possible scenarios that could be considered for the cosmic rate of short GRBs. Thus, in order to approximate the comoving rate density $\dot{\zeta}(z)$ of SGRBs, we adopt the Star Formation Rate (SFR) model, $\dot{\zeta}$, described in Amir Shahmoradi and Robert J Nemiroff, 2015 in the form of a piecewise power-law function,

$$\dot{\zeta}(z) \propto \begin{cases} (1+z)^{\gamma_0} & z < z_0 \\ (1+z)^{\gamma_1} & z_0 < z < z_1 \\ (1+z)^{\gamma_2} & z > z_1\,, \end{cases} \tag{3.15}$$

with parameters,

$$\boldsymbol{\theta}_z = (z_0, z_1, \gamma_0, \gamma_1, \gamma_2) = (0.993, 3.8, 3.3, 0.055, -4.46) \tag{3.16}$$

This SFR model is then convolved with a log-normal model of the delay time distribution (e.g., Amir Shahmoradi and Robert J Nemiroff, 2015),

$$\mathcal{LN}(\tau|\mu,\sigma) \propto \frac{1}{\tau\sigma} e^{-\frac{(\ln\tau-\mu)^2}{2\sigma^2}} \tag{3.17}$$

with parameters $[\mu,\sigma] = [\log(0.1), 1.12]$ in units of billion years (Gyrs) adopted from (e.g., Amir Shahmoradi and Robert J Nemiroff, 2015), such that the comoving rate density of SGRBs is calculated as,

$$\dot{\zeta}(z) \propto \int_z^\infty \mathcal{SFR}(z')\mathcal{LN}\big(t(z)-t(z')\big)\frac{\mathrm{d}t}{\mathrm{d}z'}\mathrm{d}z', \tag{3.18}$$

with the universe's age $t(z)$ at redshift z given by,

$$t(z) = \frac{1}{H_0}\int_z^\infty \frac{dz'}{(1+z')\sqrt{(1+z')^3\Omega_M+\Omega_\Lambda}}, \tag{3.19}$$

3.3.3 The SGRB Properties Rate Model: $\mathcal{R}_{tru}^{\mathrm{g}}$

As for the choice of the statistical model for the joint distribution of the four main intrinsic properties of SGRBs, $\boldsymbol{D}_{\mathrm{int}}^{\mathrm{g}}$, a multivariate log-normal distribution, $\mathcal{R}_{tru}^{\mathrm{g}} \equiv \mathcal{LN}$, is assumed in this work, whose parameters (i.e., the mean vector and the covariance matrix), $\boldsymbol{\theta}_{tru}^{\mathrm{g}} = \{\boldsymbol{\mu}, \boldsymbol{\Sigma}\}$, will have to be constrained by data. The justification for the choice of a multivariate log-normal as the underlying intrinsic population distribution of SGRBs is multi-folded. First, the observed joint distribution of BATSE SGRB properties highly resembles a log-normal shape that is censored close to the detection threshold of BATSE. Second, unlike power-law distribution which has traditionally been the default choice of model for the luminosity function of SGRBs, log-normal models provide natural upper and lower bounds on the total energy budget and luminosity of SGRBs, eliminating the need for setting artificial sharp bounds on the distributions to properly normalize them. Third, log-normal along with Gaussian distribution, are among the most naturally-occurring statistical distributions in nature, whose generalizations to multi-dimensions are also well studied and understood. This is a highly desired property especially for our work, given the overall mathematical and computational complexity of the model proposed and developed here.

3.3.4 The BATSE Detection Threshold: η_{eff}

Compared to Fermi Gamma-Ray Burst Monitor (C. Meegan et al., 2009) and Neil Gehrels Swift Observatory (Gehrels et al., 2004; Lien et al., 2016), BATSE had a relatively simple triggering algorithm. The BATSE detection efficiency and algorithm have been already extensively studied by the BATSE team as well as independent authors (e.g., Amir Shahmoradi and Robert J Nemiroff, 2010; Shahmoradi and Nemiroff, 2011a; Amir Shahmoradi, 2013a; Amir Shahmoradi and Robert J Nemiroff, 2015). However, simple implementation and usage of the known BATSE trigger threshold for modeling the BATSE catalog's sample incompleteness can lead to systematic biases in the inferred quantities of interest. BATSE triggered on 2702 GRBs, out of which only 2145, or approximately 79%, have been consistently analyzed and reported in the current BATSE catalog, with the remaining 21% either having a low accumulation of count rates or missing a full spectral/temporal coverage (Amir Shahmoradi and Robert J Nemiroff, 2015). Thus, the extent of sample incompleteness in the BATSE catalog is likely not fully and accurately represented by the BATSE triggering algorithm alone.

BATSE LADs generally triggered on a GRB if the number of photons per 64, 256, or 1024 [ms] arriving at the detectors in $50 - 300$ [keV] energy window, P_{ph}, reached a certain threshold in units of the background photon count fluctuations, σ. This threshold was typically set to 5.5σ during much of BATSE's operational lifetime. However, the naturally-occurring fluctuations in the average background photon counts effectively lead to a monotonically increasing BATSE detection efficiency as a function of P_{ph}, instead of a sharp cutoff on the observed P_{ph} distribution of SGRBs.

Although the detection efficiency of most gamma-ray detectors depends solely on the observed peak *photon* flux in a limited energy window, the quantity of interest that is most often modeled and studied is the *bolometric* peak 'energy' flux (P_{bol}). This variable depends on the observed peak photon flux and the spectral peak energy (E_{p}) for the class of LGRBs (e.g., Amir Shahmoradi, 2013a), also on the observed duration (e.g., T_{90}) of the burst for the class of SGRBs (Amir Shahmoradi and Robert J Nemiroff, 2015). The effects of GRB duration on the peak flux measurement is very

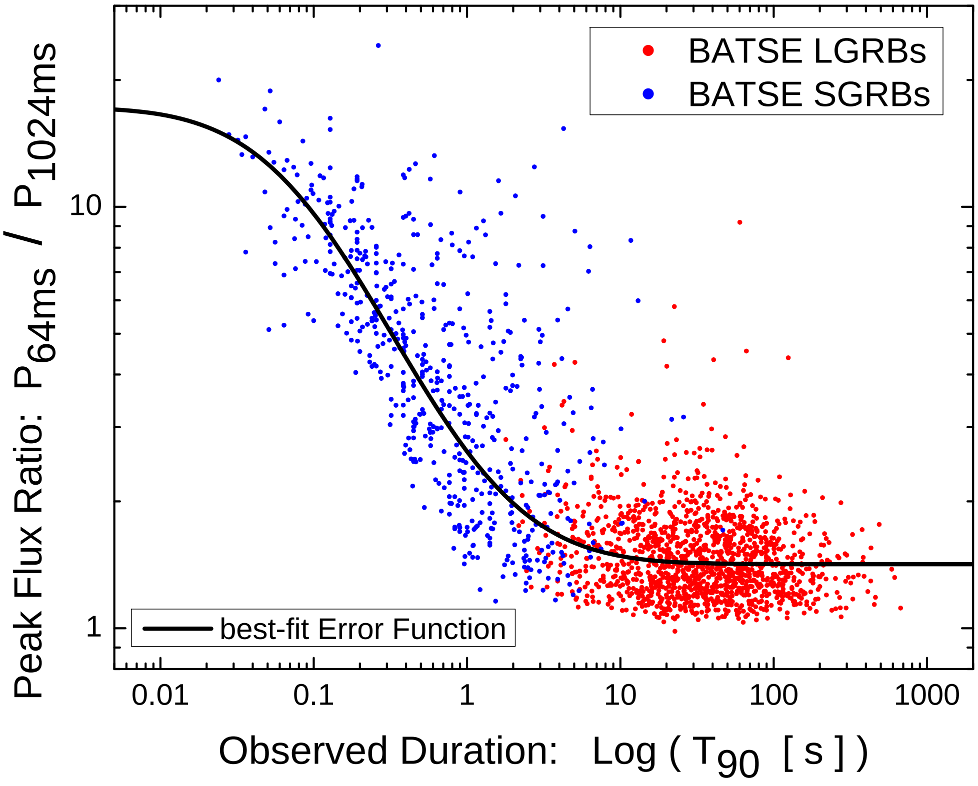

FIGURE 3.3: An illustration of the higher detection probability of short GRBs on 64*ms* timescale peak flux towards very short durations compared to the commonly used 1024*ms* peak flux definition for LGRBs. The duration-dependence of the ratio of the two peak flux definitions highlights the inadequacy of the conventional definition of peak flux based on 1024*ms* time binning for the detection of short GRBs.

well illustrated in the *left* plot of Figure 4.2, where it is shown that for BATSE GRBs with $T_{90} \lesssim 1024ms$, the timescale used for the definition of the peak flux does indeed matter. This is particularly important in modeling the triggering algorithm of BATSE Large Area Detectors when a short burst could be potentially detected on any of the three different peak flux timescales used in the triggering algorithm: 64*ms*, 256*ms* & 1024*ms*. Therefore, the following approach from Amir Shahmoradi and Robert J Nemiroff (2015) is adopted to construct a minimally-biased model of BATSE trigger efficiency for the population study of short-hard bursts.

First, since only one definition (i.e., timescale) of the bolometric peak flux can be incorporated in the SGRB world model, we use the least biased definition of peak flux for SGRBs – the 64*ms* timescale definition – in the GRB world model. Although, this definition is duration-independent for virtually all BATSE GRBs, it becomes an increasingly biased measure of the peak flux for very long duration GRBs ($T_{90} \gg 1s$) close to the detection threshold. We then approximate the 3 *discrete* timescale trigger efficiency of BATSE LADs with a sigmoidal function that increases monotonically with increasing duration of the burst, from 64*ms* to 1024*ms*. In other words, we convert the 64*ms* peak flux used in our GRB world model to an effective *triggering* peak flux $P_{\rm eff}$ $[ergs\ s^{-1}]$, for which the detection efficiency of BATSE becomes duration-independent.

To expand on this, consider an idealized GRB lightcurve containing only a single square-shaped pulse with an exact duration of 64ms and a signal strength that is 4 times the required significance for its detection on a 64ms peak flux timescale. In contrast, if there were only one triggering timescale 1024ms available on BATSE, the signal strength of this 64ms event would fall right on the detection threshold of BATSE LADs. Thus, a 64ms burst of peak flux P_{64} $[ph\ s^{-1}]$ would be equivalent to an effective 1024ms peak flux,

$$P_{\rm eff}\ [ph\ s^{-1}] = \frac{1}{4} P_{64}\ [ph\ s^{-1}], \tag{3.20}$$

for the triggering algorithm of BATSE on a 1024ms timescale.

In reality however, GRB lightcurves are far more diverse than a single square pulse. Thus in order to build a more realistic model of BATSE LAD triggering algorithm, we fit a *complementary* Error function of the mathematical form,

$$\mathrm{erfc}(x) = \frac{2}{\sqrt{\pi}} \int_x^\infty \mathrm{e}^{-t^2}\, dt, \tag{3.21}$$

to the logarithm of the ratio of 64ms to 1024ms peak fluxes ($R_{\mathrm{P}_{64}/\mathrm{P}_{1024}}$) as a function of the observed duration (T_{90}) of BATSE GRBs, as illustrated in the *left plot* of Figure 4.2. The resulting best-fit function for $R_{\mathrm{P}_{64}/\mathrm{P}_{1024}}$ has the form,

$$\begin{aligned} \log\left(R_{\mathrm{P}_{64}/\mathrm{P}_{1024}}\right) &\simeq 0.15 \\ &+ 0.56 \times \mathrm{erfc}\left(\frac{\log\left(T_{90}\right) + 0.48}{1.05}\right). \end{aligned} \tag{3.22}$$

The effective *triggering* peak flux in the SGRB world model is then calculated using the following relation,

$$\log\left(P_{\rm eff}\right) \simeq \log\left(P_{64}\right) - \frac{1}{2}\left(\log\left(R_{\mathrm{P}_{64}/\mathrm{P}_{1024}}\right) - 0.15\right). \tag{3.23}$$

Once $P_{\rm eff}$ is obtained, the approach of Amir Shahmoradi (2013a) is followed to calculate the detection probability (η) of a given SGRB with an effective *triggering* peak flux $P_{\rm eff}$,

$$\begin{aligned} &\eta\left(\,\text{detection}\,|\mu_{\rm thresh}, \sigma_{\rm thresh}, L_{\rm iso}, E_{\rm pz}, T_{\rm 90z}, z\right) \\ &= \frac{1}{2} + \frac{1}{2} \times \\ &\mathrm{erf}\left(\frac{\log\left(P_{\rm eff}(L_{\rm iso}, E_{\rm pz}, T_{\rm 90z}, z) - \mu_{\rm thresh}\right)}{\sqrt{2}\sigma_{\rm thresh}}\right), \end{aligned} \tag{3.24}$$

where $\mu_{\rm thresh}$ & $\sigma_{\rm thresh}$ are the detection threshold parameters that are found by fitting the SGRB world model to BATSE observational data, and $P_{\rm eff}(L_{\rm iso}, E_{\rm pz}, T_{\rm 90z}, z)$ is the 1024ms effective triggering peak flux in BATSE energy range of detection , 50–300[keV], calculated from the 64ms peak flux ($P_{64}(L_{\rm iso}, E_{\rm pz}, z)$ $[ph\ s^{-1}]$) in BATSE detection energy range using (3.23). The connection between the rest-frame GRB parameters, $L_{\rm iso}\&E_{\rm pz}, z$, and the 64$ms$ peak flux P_{64} is obtained by fitting a smoothly broken power-law known as the Band model (Band et al., 1993) of the mathematical form,

$$\Phi(E) \propto \begin{cases} E^{\alpha}\ \mathrm{e}^{\left(-\frac{(1+z)(2+\alpha)E}{E_{\mathrm{pz}}}\right)} & \text{if } E \leq \left(\frac{E_{\mathrm{pz}}}{1+z}\right)\left(\frac{\alpha-\beta}{2+\alpha}\right), \\ E^{\beta} & \text{if otherwise.} \end{cases} \tag{3.25}$$

to SGRBs differential photon spectra, such that,

$$P_{64}\left(L_{\mathrm{iso}}, E_{\mathrm{pz}}, z\right) = \frac{L_{\mathrm{iso}}}{4\pi {D_L}^2(z)} \frac{\int_{50}^{300} \Phi \ \mathrm{d}\,E}{\int_{0.1/1+z}^{20000/1+z} E\Phi \ \mathrm{d}\,E}, \tag{3.26}$$

where $d_L(z)$ is the cosmological luminosity distance. In order to bring the above calculations into the realm of current computational technologies, we simplify the integration limits in the denominator of (3.26) to a redshift-independent energy range $[0.1\mathrm{keV}, 20\mathrm{MeV}]$ and fix the low– & high– energy photon indices of the Band model of (3.25) to their corresponding population averages $\alpha = -1.1$ & $\beta = -2.3$. Amir Shahmoradi (2013a) and Amir Shahmoradi and Robert J Nemiroff (2015) shows that these simplifications result in uncertainty of < 0.05dex in the estimated peak flux, which is negligible compared to the existing systematic biases in BATSE data. The interested reader is referred to Appendix to the uncertainties in the spectral peak energy estimates of Amir Shahmoradi and Robert J Nemiroff (2010) used in this work.

Chapter 4

Results

4.1 The Cosmic Rate Model Fitting

Now, with a statistical model at hand for the observed rate of short GRBs, we proceed by first fitting the proposed censored cosmic SGRB rate model, $\mathcal{R}_{cen}$ to 565 BATSE SGRB data under the redshift distribution scenario prescribed in the previous section. The posterior PDF of parameters of the cosmic rate model of SGRBs is explored by a *Parallel Delayed-Rejection Adaptive Metropolis-Hastings Markov Chain Monte Carlo algorithm* (the *ParaDRAM* algorithm) that we have developed for such sampling tasks as part of a larger Monte Carlo simulation package named ParaMonte available in C/C++/Fortran/MATLAB/Python programming languages* (e.g., Amir Shahmoradi, 2013a; Amir Shahmoradi, 2013b; Amir Shahmoradi, 2014; Amir Shahmoradi and Robert J Nemiroff, 2015; A. Shahmoradi and R. J. Nemiroff, 2017a; A. Shahmoradi and R. J. Nemiroff, 2017b; Amir Shahmoradi, 2018; Amir Shahmoradi, 2019; Kumbhare and Amir Shahmoradi, 2020; Amir Shahmoradi, Bagheri, and Kumbhare, 2020).

However, due to the complex truncation imposed on SGRB data and the world model by the BATSE detection threshold, maximization of the posterior distribution of the parameters of the cosmic rate model of SGRBs is not only analytically intractable but also computationally, extremely complex. Calculation of the posterior distribution as given by (3.14) requires a multivariate integral over the 4-dimensional space of SGRB variables at any given redshift. In addition, due to lack of redshift (z) information for BATSE SGRBs, the probability for observation of each SGRB given the model parameters must be marginalized over all possible redshifts, adding another layer of integration to the 4-dimensional integration. These numerical integrations make sampling from the posterior distribution of the parameters of the SGRBs cosmic rate model an extremely difficult task. Therefore, the inclusion of the measurement uncertainties, which would make the computations far more complex, were not considered in this work.

The joint posterior distribution of the model parameters is then obtained by iterative sampling using a variant of Markov Chain Monte Carlo (MCMC) techniques known as Adaptive Metropolis-Hastings (e.g., Haario, Saksman, Tamminen, et al., 2001). To further the efficiency of MCMC sampling, we implement all algorithms in Fortran (Backus, 1978; Metcalf, Reid, and Cohen, 2011), and approximate the numerical integration in the definition of the luminosity distance of Eqn. 2.5 by the analytical expressions of Wickramasinghe and Ukwatta (2010). This integration is encountered on the order of billion times during the MCMC sampling of the posterior distribution.

---

*Available at: `https://github.com/cdslaborg/paramonte`

The computations are performed on 96 processors in parallel on two Skylake compute-nodes of the Stampede2 supercomputer at Texas Advanced Computing Center. Extensive tests we performed to ensure a high level of accuracy of the high-dimensional numerical integrations involved in the derivation of the posterior distribution of the parameters of the censored cosmic rate model for SGRBs as given in (3.14). The resulting best-fit parameters the cosmic SGRB rate model are summarized in 4.1, and the marginal distributions of their parameters are compared with each other in Figure 4.1.

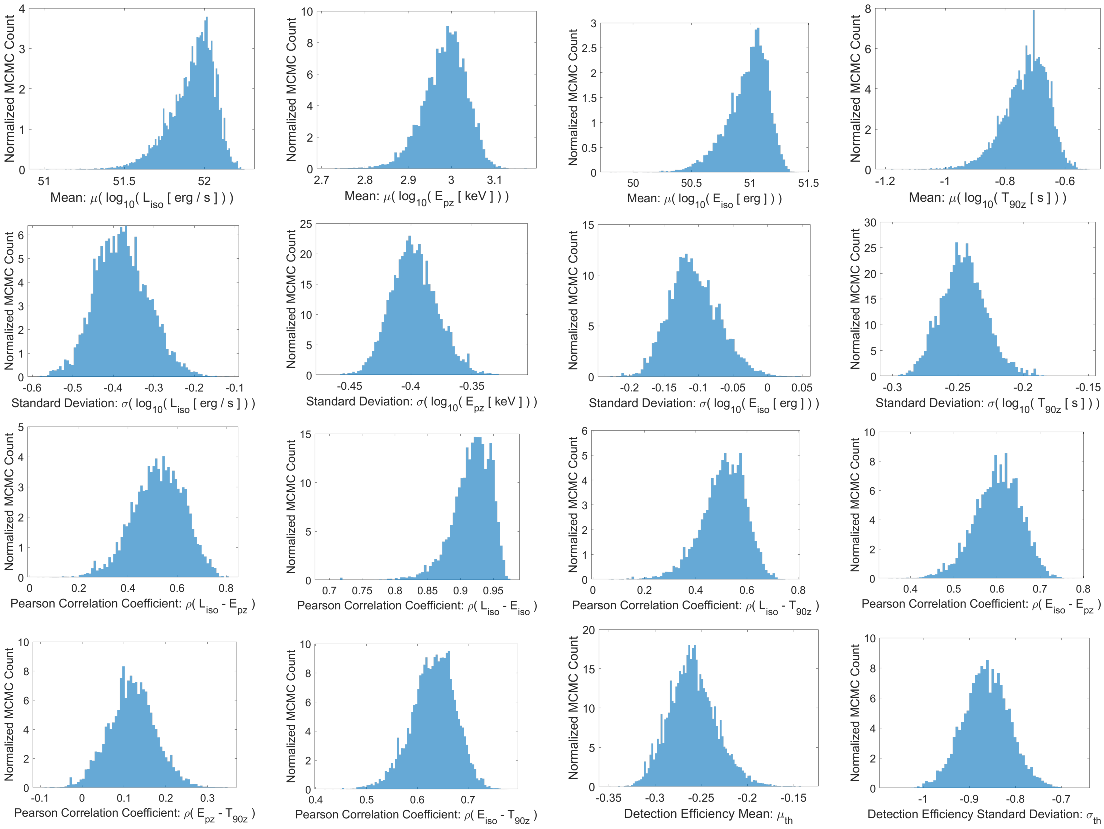

FIGURE 4.1: The marginal posterior distributions of the 16 parameters of the SGRB world model, for the cosmic SGRB redshift distribution of Amir Shahmoradi and Robert J Nemiroff, 2015 considered in this work.

Once the parameters of the censored cosmic rate model (3.7) are constrained, we use the calibrated model at the second level of the analysis to further constrain the PDFs of the unknown redshifts of individual BATSE LGRBs according to (3.12). Similar to the Empirical Bayes methodology, this iterative process can continue until convergence to a specific set of redshift PDFs occurs. However, given the computational complexity and the expense of each iteration, the iterative refinement process is stopped after obtaining the first round of estimates. This is also a common practice in the Empirical Bayes modeling.

The mean redshifts together with 50% and 90% prediction intervals for the three rate density scenarios are also reported in Table 5. On average, the redshifts of individual BATSE SGRBs can be constrained to within a 50% uncertainty range of 0.51. At 90% confidence level, the prediction intervals expand to wider a uncertainty range of 1.31. Figure 4.2 shows the derived Probability Density Functions (PDFs) of

TABLE 4.1: Mean best-fit parameters of SGRB World Model, compared to LGRB world model of Amir Shahmoradi (2013a).

Parameter	SGRBs World Model	LGRBs World Model
Redshift Parameters (Equation 3.15)		
z_0	0.993	0.993
z_1	3.8	3.8
γ_0	3.3	3.3
γ_1	0.0549	0.0549
γ_2	-4.46	-4.46
Log-normal Merger Delay (Equation 3.17)		
μ_{delay}	0.1	–
σ_{delay}	1.12	–
Location Parameters		
$\log_{10}(L_{\rm iso})$	51.88 ± 0.16	51.54 ± 0.18
$\log_{10}(E_{\rm iso})$	50.93 ± 0.19	51.98 ± 0.18
$\log_{10}(E_{\rm pz})$	2.98 ± 0.05	2.48 ± 0.05
$\log_{10}(T_{\rm 90z})$	-0.74 ± 0.08	1.12 ± 0.03
Scale Parameters		
$\log_{10}(\sigma_{L_{\rm iso}})$	-0.36 ± 0.06	-0.25 ± 0.06
$\log_{10}(\sigma_{E_{\rm iso}})$	-0.10 ± 0.04	-0.08 ± 0.03
$\log_{10}(\sigma_{E_{\rm pz}})$	-0.39 ± 0.02	-0.44 ± 0.02
$\log_{10}(\sigma_{T_{\rm 90z}})$	-0.24 ± 0.02	-0.37 ± 0.01
Correlation Coefficients		
$\rho_{L_{\rm iso}-E_{\rm iso}}$	0.91 ± 0.03	0.94 ± 0.01
$\rho_{L_{\rm iso}-E_{\rm pz}}$	0.51 ± 0.10	0.45 ± 0.07
$\rho_{L_{\rm iso}-T_{\rm 90z}}$	0.50 ± 0.09	0.48 ± 0.09
$\rho_{E_{\rm iso}-E_{\rm pz}}$	0.60 ± 0.06	0.58 ± 0.04
$\rho_{E_{\rm iso}-T_{\rm 90z}}$	0.63 ± 0.05	0.60 ± 0.05
$\rho_{E_{\rm pz}-T_{\rm 90z}}$	0.12 ± 0.06	0.31 ± 0.04
BATSE Detection Efficiency (Eqn. 3.24)		
μ_{thresh}	-0.25 ± 0.03	-0.45 ± 0.02
$\log_{10}(\sigma_{thresh})$	-0.86 ± 0.05	-0.90 ± 0.05

a subset of 565 BATSE SGRBs. As illustrated, the redshifts of some BATSE events can be better constrained than other events.

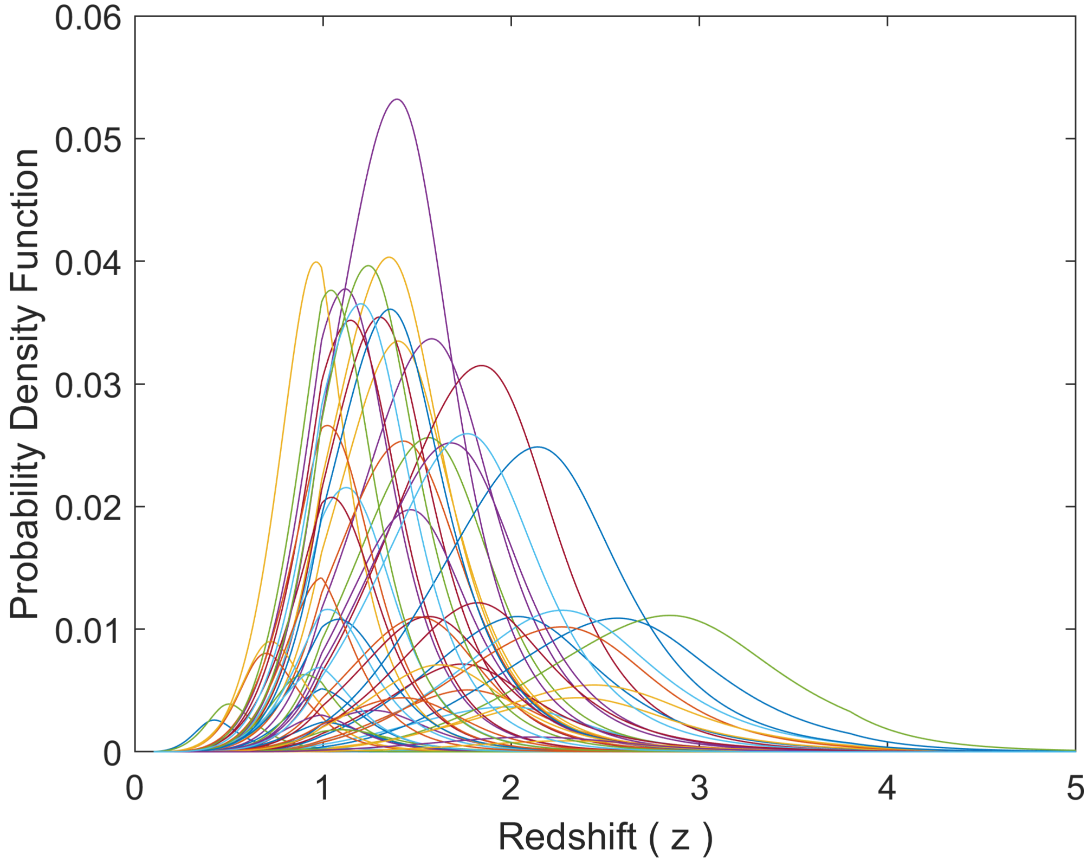

FIGURE 4.2: An illustration of the derived Probability Density Functions (PDFs) of a subset of 565 BATSE SGRBs. Each curve corresponds to the inferred likelihood of different values of redshift (z) for a single BATSE SGRB.

Chapter 5

Discussion and Concluding Remarks

In this work, a semi-Bayesian methodology was proposed to infer the unknown redshifts of 565 BATSE catalog SGRBs. Towards this, first, the two populations of BATSE LGRBs and SGRBs were segregated using the fuzzy C-means classification method based on the observed duration and spectral peak energies of 1966 BATSE GRBs with available spectral and temporal information. Then the process of SGRB detection was modeled as a non-homogeneous spatiotemporal Poisson process, whose rate parameter is modeled by a multivariate log-normal distribution as a function of the four main SGRB intrinsic attributes: the 1024 [ms] isotropic peak luminosity (L_{iso}), the total isotropic emission (E_{iso}), the intrinsic spectral peak energy (E_{pz}), and the intrinsic duration (T_{90z}). To calibrate the parameters of the rate model, a fundamental assumption was made: SGRBs trace the Cosmic Star Formation Rate (SFR) convolved with a model for the binary Neutron star merger delay distribution. Then the resulting posterior probability densities of the model parameters were used to compute the probability density functions of the redshifts of individual BATSE LGRBs.

The major conclusion of this work is that, although sample incompleteness may strongly affect an observational dataset, the Bayesian probability theory can enable us to overcome the limitations of the observational sample by constraining the unknowns and biases present in the dataset via our prior knowledge of different aspects of the problem at hand.

While being a remote possibility, one of the potential caveats of the presented redshift estimates catalog is that, if an LGRB has been mistakenly classified as an SGRB in this catalog of 565 by the fuzzy C-means classification method, then its estimated redshift may not be accurate. Also, this work did not take into account the potential effects of the GRBs' jet beaming angle. A recent study by Lazzati et al. (2013) finds that the different orientations of the GRB jet axis with respect to the observer could partially explain the observed GRB brightness-hardness type relations. Such an effect could potentially lead to more uncertainty in the predicted redshifts. These are among improvements that could be made in the future to the presented mathematically-rigorous, purely-probabilistic, bias-aware approach to estimating or further constraining the unknown redshifts of GRBs in the currently-available and future GRB catalogs.

BATSE 565 SGRB Redshift Estimates

Trigger	mean(z)	mode(z)	$Q_{5\%}(z)$	$Q_{25\%}(z)$	$Q_{50\%}(z)$	$Q_{75\%}(z)$	$Q_{95\%}(z)$
108	1.62	1.58	1.05	1.35	1.58	1.85	2.30
138	1.50	1.47	0.99	1.26	1.48	1.71	2.12
185	1.08	1.02	0.70	0.91	1.06	1.23	1.54
207	0.77	0.75	0.50	0.64	0.76	0.88	1.09
218	1.89	1.86	1.24	1.59	1.86	2.15	2.64
229	1.39	1.36	0.92	1.17	1.36	1.58	1.95
254	1.22	1.17	0.83	1.03	1.19	1.37	1.70
289	0.84	0.83	0.54	0.70	0.83	0.96	1.18
297	1.04	0.99	0.70	0.89	1.02	1.17	1.43
373	1.34	1.30	0.89	1.12	1.31	1.52	1.89
432	0.56	0.53	0.35	0.46	0.55	0.65	0.82
474	0.46	0.43	0.29	0.37	0.44	0.52	0.67
480	0.56	0.53	0.36	0.46	0.55	0.64	0.82
486	1.21	1.16	0.80	1.02	1.18	1.38	1.71
491	1.18	1.13	0.78	0.99	1.15	1.35	1.68
508	1.49	1.45	0.98	1.24	1.46	1.69	2.10
512	0.69	0.66	0.43	0.57	0.67	0.79	0.99
537	1.65	1.61	1.09	1.39	1.62	1.88	2.33
547	1.02	0.99	0.69	0.87	1.00	1.15	1.41
551	0.77	0.75	0.50	0.65	0.76	0.88	1.09
555	1.22	1.16	0.81	1.02	1.18	1.38	1.72
568	0.80	0.79	0.53	0.68	0.79	0.92	1.13
575	0.97	0.98	0.65	0.83	0.96	1.10	1.35
603	0.84	0.83	0.55	0.71	0.83	0.96	1.18
677	0.48	0.46	0.30	0.40	0.47	0.56	0.71
729	0.87	0.86	0.56	0.73	0.86	0.99	1.22
734	1.32	1.27	0.88	1.11	1.29	1.51	1.87
788	1.11	1.04	0.73	0.93	1.08	1.25	1.57
799	0.93	0.93	0.59	0.78	0.92	1.06	1.33
809	1.01	0.99	0.67	0.86	0.99	1.13	1.40
830	0.68	0.66	0.44	0.57	0.67	0.78	0.98
834	2.48	2.47	1.61	2.09	2.45	2.83	3.46
836	1.37	1.34	0.90	1.15	1.34	1.55	1.92
845	2.05	2.02	1.34	1.72	2.02	2.33	2.88
856	1.18	1.13	0.78	0.99	1.15	1.35	1.68
867	1.65	1.60	1.08	1.38	1.61	1.88	2.34

Continued on Next Page . . .

Table 0 – Continued

Trigger	mean(z)	mode(z)	$Q_{5\%}$(z)	$Q_{25\%}$(z)	$Q_{50\%}$(z)	$Q_{75\%}$(z)	$Q_{95\%}$(z)
878	1.05	0.99	0.70	0.89	1.03	1.18	1.46
906	1.06	1.00	0.72	0.90	1.04	1.19	1.47
909	2.89	2.89	1.90	2.44	2.85	3.30	3.96
929	1.59	1.56	1.05	1.34	1.56	1.81	2.23
936	0.91	0.91	0.61	0.78	0.90	1.03	1.27
942	2.36	2.34	1.54	1.99	2.33	2.69	3.31
974	2.76	2.76	1.82	2.33	2.73	3.15	3.79
1051	1.17	1.13	0.78	0.99	1.15	1.33	1.65
1073	1.10	1.04	0.74	0.93	1.08	1.24	1.53
1076	0.61	0.59	0.39	0.51	0.60	0.70	0.89
1088	0.47	0.44	0.30	0.39	0.46	0.54	0.69
1096	1.11	1.05	0.73	0.93	1.09	1.27	1.58
1097	0.97	0.98	0.64	0.83	0.96	1.10	1.36
1102	0.94	0.94	0.62	0.79	0.92	1.06	1.30
1112	1.40	1.36	0.93	1.18	1.37	1.58	1.95
1128	1.27	1.23	0.83	1.06	1.24	1.45	1.80
1129	1.79	1.78	1.17	1.51	1.76	2.04	2.52
1154	0.92	0.92	0.61	0.78	0.91	1.04	1.28
1211	1.21	1.17	0.81	1.02	1.19	1.37	1.70
1223	1.72	1.68	1.11	1.43	1.69	1.97	2.47
1289	1.23	1.18	0.83	1.03	1.20	1.39	1.72
1308	0.84	0.83	0.53	0.70	0.83	0.96	1.18
1346	1.63	1.59	1.07	1.36	1.60	1.86	2.30
1359	1.02	0.99	0.68	0.87	1.00	1.14	1.41
1404	1.90	1.88	1.24	1.60	1.87	2.17	2.67
1435	2.19	2.17	1.40	1.83	2.15	2.50	3.08
1443	1.32	1.24	0.87	1.09	1.28	1.50	1.89
1453	0.56	0.54	0.36	0.46	0.55	0.65	0.82
1461	0.93	0.92	0.61	0.78	0.91	1.05	1.30
1481	1.81	1.74	1.15	1.49	1.76	2.08	2.64
1518	1.16	1.11	0.79	0.98	1.13	1.31	1.62
1546	1.05	0.99	0.68	0.88	1.02	1.19	1.51
1553	0.71	0.68	0.46	0.59	0.69	0.81	1.01
1566	0.87	0.86	0.57	0.73	0.86	0.99	1.21
1588	0.91	0.91	0.61	0.78	0.90	1.03	1.27
1634	1.23	1.18	0.83	1.04	1.20	1.39	1.71

Continued on Next Page . . .

Table 0 – Continued

Trigger	mean(z)	mode(z)	$Q_{5\%}$(z)	$Q_{25\%}$(z)	$Q_{50\%}$(z)	$Q_{75\%}$(z)	$Q_{95\%}$(z)
1635	1.14	1.09	0.76	0.96	1.11	1.29	1.59
1636	1.95	1.88	1.24	1.61	1.91	2.24	2.83
1637	1.80	1.78	1.15	1.51	1.77	2.06	2.56
1659	1.44	1.41	0.96	1.21	1.41	1.63	2.01
1662	1.13	1.08	0.75	0.96	1.10	1.27	1.57
1665	0.56	0.53	0.35	0.46	0.54	0.64	0.81
1679	3.51	3.69	2.38	3.03	3.50	3.94	4.72
1680	1.03	0.99	0.68	0.87	1.01	1.16	1.44
1683	1.36	1.27	0.88	1.11	1.31	1.55	1.99
1694	1.00	0.99	0.68	0.86	0.99	1.13	1.39
1719	1.00	0.99	0.67	0.85	0.98	1.12	1.38
1736	0.93	0.93	0.60	0.78	0.92	1.06	1.32
1741	0.83	0.82	0.54	0.70	0.82	0.95	1.17
1747	1.20	1.15	0.80	1.01	1.17	1.36	1.68
1760	0.94	0.93	0.63	0.80	0.92	1.06	1.30
1851	0.82	0.80	0.54	0.69	0.80	0.93	1.14
1953	1.36	1.32	0.92	1.15	1.34	1.54	1.91
1968	1.41	1.38	0.94	1.19	1.39	1.60	1.97
2003	1.10	1.05	0.74	0.94	1.08	1.25	1.54
2037	1.11	1.03	0.74	0.93	1.08	1.25	1.57
2040	1.65	1.62	1.09	1.39	1.62	1.88	2.31
2041	1.24	1.19	0.84	1.05	1.21	1.41	1.75
2043	1.51	1.48	0.99	1.26	1.48	1.72	2.12
2044	2.20	2.16	1.42	1.83	2.16	2.51	3.12
2049	0.84	0.82	0.55	0.71	0.83	0.95	1.17
2056	2.25	2.21	1.47	1.89	2.21	2.56	3.16
2068	0.55	0.52	0.34	0.45	0.53	0.63	0.81
2099	2.40	2.36	1.57	2.02	2.36	2.74	3.39
2103	1.31	1.27	0.88	1.10	1.28	1.48	1.82
2115	1.02	0.99	0.68	0.87	1.00	1.15	1.42
2117	1.04	0.99	0.69	0.88	1.02	1.17	1.45
2125	0.50	0.47	0.31	0.41	0.48	0.57	0.73
2126	0.91	0.90	0.60	0.77	0.90	1.03	1.26
2132	0.90	0.90	0.57	0.75	0.89	1.03	1.27
2142	1.86	1.82	1.21	1.56	1.82	2.12	2.62
2145	1.40	1.37	0.93	1.18	1.37	1.59	1.96

Continued on Next Page . . .

Table 0 – Continued

Trigger	mean(z)	mode(z)	$Q_{5\%}(z)$	$Q_{25\%}(z)$	$Q_{50\%}(z)$	$Q_{75\%}(z)$	$Q_{95\%}(z)$
2146	0.99	0.99	0.66	0.84	0.98	1.12	1.37
2155	1.18	1.13	0.80	1.00	1.15	1.33	1.64
2159	1.14	1.07	0.73	0.95	1.11	1.30	1.63
2161	0.88	0.87	0.57	0.74	0.86	1.00	1.23
2163	1.46	1.43	0.97	1.23	1.43	1.66	2.04
2167	0.69	0.67	0.44	0.58	0.68	0.79	0.99
2201	1.11	1.07	0.75	0.95	1.09	1.26	1.54
2205	1.29	1.24	0.85	1.08	1.26	1.47	1.82
2206	1.10	1.05	0.74	0.94	1.08	1.24	1.52
2217	0.88	0.87	0.59	0.75	0.87	1.00	1.23
2220	1.09	1.04	0.73	0.93	1.07	1.23	1.51
2265	1.38	1.35	0.92	1.16	1.36	1.57	1.95
2268	1.49	1.43	0.98	1.24	1.45	1.70	2.13
2273	0.46	0.43	0.29	0.37	0.44	0.52	0.67
2283	1.20	1.14	0.79	1.01	1.17	1.37	1.72
2288	1.40	1.37	0.93	1.18	1.37	1.59	1.96
2312	1.07	1.01	0.72	0.91	1.05	1.21	1.48
2326	0.96	0.96	0.64	0.81	0.94	1.08	1.33
2327	2.78	2.79	1.84	2.36	2.76	3.17	3.81
2330	0.69	0.66	0.45	0.58	0.67	0.79	0.98
2332	0.96	0.97	0.63	0.81	0.95	1.09	1.35
2352	1.83	1.81	1.19	1.54	1.80	2.09	2.57
2353	1.52	1.50	1.01	1.28	1.50	1.73	2.13
2357	1.21	1.16	0.81	1.02	1.19	1.37	1.71
2358	1.40	1.36	0.91	1.16	1.37	1.59	1.98
2360	1.43	1.40	0.95	1.20	1.40	1.63	2.01
2365	1.71	1.68	1.12	1.44	1.68	1.95	2.41
2368	2.89	2.90	1.92	2.46	2.87	3.30	3.95
2372	1.15	1.11	0.77	0.98	1.13	1.31	1.61
2377	0.92	0.92	0.62	0.79	0.91	1.04	1.27
2382	3.11	3.15	2.06	2.65	3.09	3.54	4.21
2384	1.34	1.31	0.89	1.13	1.31	1.52	1.88
2395	1.00	0.99	0.65	0.84	0.98	1.13	1.39
2401	2.72	2.71	1.79	2.30	2.69	3.10	3.76
2424	2.62	2.60	1.72	2.21	2.59	2.99	3.64
2434	2.21	2.14	1.39	1.81	2.15	2.55	3.22

Continued on Next Page . . .

Table 0 – Continued

Trigger	mean(z)	mode(z)	$Q_{5\%}$(z)	$Q_{25\%}$(z)	$Q_{50\%}$(z)	$Q_{75\%}$(z)	$Q_{95\%}$(z)
2448	1.52	1.49	1.00	1.28	1.49	1.73	2.13
2449	1.06	1.00	0.71	0.90	1.04	1.20	1.47
2454	2.24	2.20	1.45	1.87	2.20	2.55	3.17
2485	1.21	1.16	0.79	1.01	1.18	1.38	1.73
2487	1.01	0.99	0.68	0.86	0.99	1.13	1.39
2502	1.03	0.99	0.69	0.88	1.01	1.15	1.42
2504	0.87	0.86	0.57	0.73	0.85	0.99	1.21
2512	0.96	0.97	0.64	0.82	0.95	1.09	1.34
2513	2.10	2.07	1.38	1.77	2.06	2.39	2.95
2523	1.40	1.37	0.94	1.18	1.37	1.59	1.96
2529	1.76	1.70	1.11	1.45	1.72	2.02	2.55
2536	1.20	1.15	0.80	1.01	1.17	1.36	1.67
2564	1.33	1.29	0.89	1.12	1.31	1.51	1.87
2583	0.60	0.58	0.38	0.50	0.59	0.69	0.87
2585	1.94	1.88	1.23	1.60	1.90	2.23	2.80
2597	1.04	0.99	0.69	0.88	1.02	1.17	1.44
2599	0.81	0.79	0.52	0.67	0.79	0.92	1.14
2614	0.60	0.57	0.39	0.50	0.59	0.69	0.87
2615	0.83	0.82	0.53	0.70	0.82	0.95	1.17
2623	1.49	1.44	0.98	1.24	1.46	1.70	2.12
2632	1.58	1.52	1.03	1.31	1.54	1.81	2.27
2633	1.62	1.59	1.06	1.36	1.59	1.85	2.28
2649	1.03	0.99	0.68	0.88	1.01	1.16	1.44
2679	0.48	0.45	0.30	0.39	0.46	0.55	0.70
2680	2.69	2.65	1.76	2.26	2.64	3.07	3.74
2690	0.87	0.86	0.57	0.74	0.86	0.99	1.21
2693	1.26	1.23	0.84	1.06	1.24	1.44	1.78
2701	1.43	1.40	0.95	1.20	1.41	1.62	2.00
2715	0.54	0.51	0.34	0.45	0.53	0.62	0.79
2728	1.41	1.36	0.94	1.18	1.37	1.60	2.00
2748	1.20	1.15	0.79	1.01	1.17	1.36	1.69
2755	1.00	0.99	0.65	0.84	0.98	1.13	1.40
2757	1.30	1.25	0.86	1.09	1.27	1.48	1.86
2760	3.07	3.10	2.01	2.59	3.04	3.52	4.22
2776	2.02	2.00	1.31	1.70	1.99	2.30	2.83
2788	1.32	1.28	0.89	1.11	1.29	1.50	1.84

Continued on Next Page . . .

Table 0 – Continued

Trigger	mean(z)	mode(z)	$Q_{5\%}$(z)	$Q_{25\%}$(z)	$Q_{50\%}$(z)	$Q_{75\%}$(z)	$Q_{95\%}$(z)
2795	0.87	0.85	0.57	0.73	0.85	0.98	1.21
2799	1.14	1.05	0.74	0.95	1.10	1.29	1.64
2800	1.45	1.41	0.96	1.22	1.42	1.64	2.02
2801	1.13	1.08	0.74	0.95	1.11	1.28	1.59
2810	2.51	2.47	1.64	2.10	2.47	2.87	3.52
2814	0.83	0.81	0.53	0.70	0.82	0.95	1.16
2821	1.12	1.07	0.74	0.95	1.10	1.27	1.58
2823	1.20	1.15	0.78	1.00	1.17	1.37	1.71
2828	1.44	1.41	0.96	1.21	1.42	1.64	2.02
2834	0.68	0.65	0.44	0.57	0.67	0.78	0.97
2844	1.95	1.92	1.26	1.63	1.92	2.23	2.76
2846	1.07	1.01	0.71	0.90	1.05	1.21	1.50
2849	2.16	2.10	1.38	1.79	2.11	2.48	3.11
2851	2.55	2.53	1.67	2.15	2.52	2.92	3.58
2860	1.30	1.25	0.88	1.09	1.27	1.47	1.82
2861	1.61	1.56	1.06	1.35	1.58	1.83	2.28
2873	1.04	0.99	0.68	0.88	1.03	1.18	1.47
2879	1.08	1.03	0.71	0.92	1.06	1.23	1.52
2892	1.03	0.99	0.67	0.87	1.01	1.16	1.45
2894	1.34	1.24	0.85	1.09	1.29	1.53	1.98
2910	0.95	0.95	0.62	0.80	0.93	1.08	1.33
2918	0.88	0.86	0.58	0.74	0.86	0.99	1.21
2933	0.63	0.61	0.41	0.53	0.62	0.73	0.92
2952	0.89	0.88	0.59	0.75	0.88	1.00	1.23
2964	1.14	1.09	0.75	0.96	1.12	1.30	1.61
2966	1.42	1.39	0.95	1.19	1.39	1.61	1.99
2973	1.21	1.17	0.81	1.03	1.19	1.37	1.70
2975	0.86	0.84	0.56	0.72	0.84	0.98	1.19
2977	1.09	1.03	0.73	0.93	1.07	1.22	1.51
2978	0.67	0.64	0.42	0.55	0.65	0.77	0.96
2987	1.32	1.28	0.89	1.11	1.29	1.50	1.84
2988	0.89	0.88	0.59	0.75	0.88	1.01	1.24
2995	0.83	0.81	0.54	0.70	0.82	0.95	1.16
3016	1.34	1.27	0.83	1.08	1.30	1.54	1.99
3027	0.75	0.72	0.48	0.62	0.73	0.86	1.06
3037	0.81	0.80	0.52	0.68	0.80	0.93	1.15

Continued on Next Page . . .

Table 0 – Continued

Trigger	mean(z)	mode(z)	$Q_{5\%}$(z)	$Q_{25\%}$(z)	$Q_{50\%}$(z)	$Q_{75\%}$(z)	$Q_{95\%}$(z)
3038	1.19	1.15	0.81	1.01	1.17	1.35	1.66
3039	1.29	1.20	0.83	1.05	1.25	1.48	1.91
3043	1.22	1.15	0.79	1.01	1.18	1.39	1.76
3051	0.78	0.75	0.48	0.64	0.76	0.90	1.13
3066	0.95	0.95	0.63	0.81	0.94	1.07	1.31
3073	0.91	0.91	0.59	0.77	0.90	1.03	1.27
3078	0.88	0.87	0.58	0.75	0.87	1.00	1.23
3087	0.76	0.73	0.48	0.63	0.74	0.88	1.10
3094	1.15	1.10	0.77	0.97	1.12	1.29	1.59
3113	1.05	0.99	0.71	0.89	1.03	1.18	1.45
3114	1.80	1.78	1.17	1.51	1.78	2.06	2.53
3118	1.12	1.07	0.75	0.95	1.09	1.26	1.55
3121	1.43	1.40	0.96	1.21	1.41	1.63	2.00
3137	0.99	0.99	0.66	0.84	0.98	1.12	1.39
3144	3.51	3.69	2.37	3.03	3.49	3.94	4.71
3146	2.62	2.59	1.71	2.20	2.58	3.00	3.68
3152	0.55	0.52	0.35	0.45	0.54	0.63	0.81
3155	2.34	2.27	1.50	1.93	2.28	2.68	3.35
3160	2.05	2.02	1.34	1.73	2.02	2.34	2.88
3164	2.75	2.71	1.79	2.31	2.71	3.15	3.83
3173	0.48	0.46	0.30	0.40	0.47	0.55	0.70
3215	0.56	0.53	0.36	0.46	0.55	0.64	0.81
3218	0.75	0.73	0.48	0.62	0.74	0.86	1.07
3266	0.90	0.89	0.59	0.76	0.89	1.02	1.25
3278	1.81	1.79	1.18	1.52	1.78	2.07	2.55
3280	2.58	2.57	1.69	2.17	2.55	2.94	3.59
3282	0.78	0.76	0.50	0.65	0.77	0.90	1.10
3286	1.07	0.99	0.69	0.89	1.05	1.22	1.55
3293	1.11	1.05	0.74	0.94	1.08	1.25	1.54
3294	1.50	1.46	0.99	1.26	1.47	1.71	2.12
3297	0.85	0.83	0.56	0.72	0.84	0.96	1.18
3308	1.58	1.56	1.04	1.33	1.55	1.80	2.21
3323	1.13	1.09	0.77	0.96	1.11	1.28	1.58
3333	0.89	0.89	0.56	0.74	0.88	1.01	1.25
3335	1.76	1.74	1.15	1.48	1.73	2.01	2.47
3338	0.88	0.88	0.55	0.73	0.87	1.01	1.26

Continued on Next Page . . .

Table 0 – Continued

Trigger	mean(z)	mode(z)	$Q_{5\%}(z)$	$Q_{25\%}(z)$	$Q_{50\%}(z)$	$Q_{75\%}(z)$	$Q_{95\%}(z)$
3340	1.15	1.10	0.78	0.98	1.13	1.30	1.60
3342	0.93	0.93	0.62	0.79	0.92	1.06	1.30
3349	0.97	0.98	0.64	0.83	0.96	1.10	1.35
3359	1.05	0.99	0.71	0.90	1.03	1.18	1.46
3374	1.22	1.18	0.82	1.03	1.19	1.38	1.70
3379	1.25	1.21	0.84	1.05	1.22	1.41	1.74
3384	0.84	0.83	0.52	0.69	0.83	0.96	1.19
3437	0.96	0.96	0.62	0.80	0.94	1.09	1.37
3441	1.00	0.99	0.66	0.85	0.99	1.13	1.40
3476	1.37	1.32	0.89	1.14	1.34	1.56	1.96
3477	1.72	1.70	1.13	1.45	1.69	1.96	2.41
3487	1.17	1.13	0.79	0.99	1.15	1.33	1.64
3494	1.38	1.34	0.92	1.16	1.35	1.56	1.93
3502	1.06	1.01	0.72	0.91	1.05	1.20	1.47
3510	1.05	0.99	0.70	0.89	1.03	1.19	1.47
3530	1.92	1.87	1.24	1.60	1.88	2.19	2.72
3545	1.44	1.41	0.96	1.21	1.41	1.63	2.02
3606	1.14	1.09	0.77	0.97	1.11	1.28	1.58
3611	2.80	2.77	1.83	2.35	2.76	3.20	3.88
3640	0.97	0.98	0.64	0.82	0.96	1.10	1.36
3642	0.79	0.77	0.52	0.67	0.78	0.90	1.11
3665	0.47	0.44	0.29	0.38	0.46	0.54	0.69
3668	0.78	0.76	0.51	0.65	0.77	0.89	1.10
3722	1.19	1.14	0.80	1.00	1.16	1.34	1.66
3728	1.18	1.14	0.79	1.00	1.16	1.34	1.66
3735	0.88	0.86	0.58	0.74	0.86	0.99	1.22
3737	0.79	0.77	0.51	0.66	0.77	0.90	1.10
3742	1.18	1.13	0.79	0.99	1.15	1.34	1.66
3751	1.08	1.03	0.74	0.93	1.07	1.22	1.50
3770	0.81	0.79	0.53	0.68	0.79	0.92	1.13
3774	1.08	1.01	0.70	0.90	1.05	1.22	1.53
3782	1.12	1.06	0.73	0.94	1.09	1.27	1.59
3791	0.88	0.86	0.58	0.74	0.86	0.99	1.21
3799	0.97	0.98	0.62	0.81	0.95	1.10	1.37
3810	0.83	0.81	0.54	0.70	0.82	0.95	1.16
3866	1.23	1.16	0.82	1.03	1.20	1.40	1.74

Continued on Next Page ...

Table 0 – Continued

Trigger	mean(z)	mode(z)	$Q_{5\%}$(z)	$Q_{25\%}$(z)	$Q_{50\%}$(z)	$Q_{75\%}$(z)	$Q_{95\%}$(z)
3867	1.04	0.99	0.71	0.89	1.02	1.17	1.44
3868	1.06	1.01	0.71	0.90	1.05	1.20	1.48
3888	0.95	0.95	0.64	0.81	0.93	1.07	1.31
3889	0.67	0.64	0.42	0.55	0.65	0.77	0.96
3894	1.27	1.23	0.85	1.07	1.24	1.44	1.78
3895	1.82	1.80	1.18	1.53	1.79	2.08	2.55
3902	0.58	0.56	0.37	0.48	0.57	0.67	0.84
3904	0.98	0.99	0.64	0.83	0.97	1.11	1.38
3910	0.90	0.89	0.56	0.75	0.89	1.03	1.30
3919	1.17	1.12	0.77	0.98	1.14	1.33	1.65
3921	0.86	0.85	0.57	0.73	0.85	0.98	1.19
3936	1.28	1.20	0.84	1.05	1.24	1.46	1.86
3939	1.88	1.81	1.20	1.55	1.83	2.16	2.74
3940	1.11	1.05	0.74	0.94	1.08	1.25	1.55
4327	0.52	0.49	0.32	0.42	0.50	0.60	0.76
4660	0.97	0.98	0.66	0.83	0.96	1.10	1.35
4744	0.95	0.96	0.63	0.81	0.94	1.08	1.33
4776	0.83	0.81	0.55	0.70	0.81	0.94	1.15
4807	0.86	0.84	0.55	0.72	0.84	0.98	1.21
4871	0.78	0.76	0.50	0.65	0.77	0.90	1.11
4955	0.80	0.78	0.53	0.68	0.79	0.92	1.12
5079	1.35	1.32	0.90	1.14	1.33	1.53	1.90
5206	0.84	0.83	0.55	0.71	0.83	0.96	1.17
5212	1.01	0.99	0.68	0.86	0.99	1.13	1.39
5277	0.70	0.68	0.46	0.59	0.69	0.80	1.00
5339	0.82	0.80	0.54	0.69	0.81	0.94	1.15
5439	0.66	0.63	0.42	0.55	0.64	0.76	0.96
5448	1.13	1.07	0.75	0.95	1.10	1.27	1.58
5453	1.63	1.61	1.07	1.37	1.60	1.86	2.29
5456	1.43	1.37	0.94	1.19	1.39	1.62	2.03
5458	0.89	0.88	0.53	0.73	0.88	1.03	1.33
5459	1.17	1.12	0.77	0.98	1.15	1.33	1.66
5461	1.44	1.41	0.96	1.21	1.41	1.64	2.02
5467	1.78	1.74	1.16	1.49	1.74	2.02	2.51
5469	1.13	1.07	0.76	0.96	1.10	1.27	1.56
5471	1.12	1.06	0.75	0.95	1.09	1.26	1.57

Continued on Next Page . . .

Table 0 – Continued

Trigger	mean(z)	mode(z)	$Q_{5\%}$(z)	$Q_{25\%}$(z)	$Q_{50\%}$(z)	$Q_{75\%}$(z)	$Q_{95\%}$(z)
5485	2.63	2.62	1.73	2.22	2.59	3.00	3.65
5488	1.15	1.11	0.77	0.98	1.13	1.31	1.62
5491	1.01	0.99	0.65	0.85	0.99	1.14	1.42
5498	1.32	1.28	0.88	1.11	1.29	1.50	1.86
5499	1.32	1.28	0.89	1.11	1.29	1.50	1.84
5500	0.61	0.59	0.39	0.51	0.60	0.71	0.89
5501	1.21	1.16	0.80	1.02	1.18	1.38	1.72
5527	0.91	0.89	0.60	0.77	0.89	1.02	1.26
5528	1.13	1.08	0.77	0.96	1.11	1.27	1.57
5529	0.95	0.95	0.64	0.81	0.93	1.07	1.31
5533	0.85	0.83	0.56	0.72	0.84	0.96	1.18
5536	0.86	0.85	0.53	0.71	0.84	0.99	1.24
5537	1.40	1.37	0.94	1.18	1.38	1.59	1.96
5546	1.73	1.70	1.13	1.45	1.70	1.97	2.45
5547	1.23	1.18	0.83	1.04	1.20	1.39	1.71
5556	1.60	1.54	1.03	1.32	1.56	1.83	2.31
5560	1.27	1.23	0.85	1.07	1.24	1.44	1.78
5562	0.84	0.82	0.55	0.71	0.83	0.95	1.17
5564	0.59	0.56	0.37	0.49	0.58	0.68	0.86
5576	1.18	1.14	0.79	1.00	1.16	1.34	1.65
5592	1.07	1.02	0.71	0.91	1.05	1.21	1.50
5599	0.92	0.92	0.62	0.78	0.91	1.04	1.27
5607	0.92	0.91	0.62	0.78	0.90	1.04	1.27
5619	0.83	0.82	0.54	0.70	0.82	0.95	1.16
5620	0.88	0.87	0.55	0.73	0.86	1.01	1.26
5633	1.03	0.99	0.67	0.87	1.01	1.17	1.46
5638	1.66	1.64	1.09	1.40	1.64	1.90	2.33
5647	0.60	0.57	0.38	0.49	0.59	0.69	0.89
5650	1.45	1.41	0.96	1.21	1.42	1.64	2.03
5664	2.17	2.15	1.41	1.82	2.14	2.48	3.05
5724	1.20	1.15	0.81	1.02	1.18	1.36	1.67
5730	1.46	1.42	0.96	1.22	1.43	1.66	2.07
5733	1.04	0.99	0.68	0.88	1.01	1.17	1.45
5740	1.25	1.21	0.84	1.05	1.22	1.41	1.75
5770	1.32	1.28	0.89	1.11	1.29	1.49	1.83
5992	0.81	0.79	0.49	0.66	0.79	0.94	1.18

Continued on Next Page ...

Table 0 – Continued

Trigger	mean(z)	mode(z)	$Q_{5\%}(z)$	$Q_{25\%}(z)$	$Q_{50\%}(z)$	$Q_{75\%}(z)$	$Q_{95\%}(z)$
6091	1.42	1.34	0.91	1.16	1.37	1.63	2.09
6096	1.13	1.07	0.76	0.96	1.10	1.27	1.57
6105	0.99	0.99	0.66	0.84	0.98	1.12	1.38
6117	1.38	1.35	0.93	1.17	1.36	1.57	1.93
6120	1.00	0.99	0.67	0.85	0.98	1.13	1.38
6123	0.49	0.46	0.31	0.41	0.48	0.56	0.72
6135	2.12	2.09	1.38	1.78	2.08	2.41	2.98
6136	1.20	1.12	0.79	1.00	1.16	1.36	1.71
6145	1.07	1.01	0.72	0.91	1.05	1.20	1.48
6153	1.35	1.32	0.90	1.14	1.33	1.53	1.90
6166	0.91	0.91	0.59	0.76	0.89	1.03	1.27
6178	1.60	1.57	1.05	1.35	1.57	1.82	2.24
6180	1.43	1.40	0.95	1.20	1.41	1.63	2.02
6182	0.99	0.99	0.66	0.84	0.97	1.12	1.39
6204	0.97	0.97	0.63	0.81	0.95	1.10	1.37
6205	0.97	0.98	0.64	0.82	0.96	1.10	1.37
6215	1.01	0.99	0.68	0.86	0.99	1.14	1.41
6216	1.48	1.39	0.95	1.21	1.43	1.70	2.18
6219	0.94	0.93	0.60	0.78	0.92	1.07	1.36
6230	0.78	0.75	0.50	0.65	0.76	0.89	1.10
6237	1.15	1.11	0.77	0.98	1.13	1.31	1.61
6238	1.17	1.12	0.78	0.99	1.15	1.33	1.65
6251	1.09	1.02	0.73	0.92	1.07	1.24	1.54
6263	0.82	0.79	0.52	0.68	0.81	0.95	1.19
6265	0.74	0.72	0.48	0.62	0.73	0.85	1.05
6275	1.18	1.13	0.79	1.00	1.15	1.33	1.65
6281	1.42	1.38	0.92	1.18	1.39	1.62	2.03
6284	1.18	1.14	0.79	1.00	1.16	1.34	1.65
6292	1.18	1.12	0.78	0.99	1.15	1.34	1.68
6299	0.93	0.92	0.60	0.78	0.91	1.05	1.31
6301	1.55	1.51	1.03	1.30	1.51	1.75	2.16
6307	1.30	1.26	0.87	1.09	1.27	1.47	1.81
6314	2.15	2.11	1.40	1.80	2.11	2.46	3.06
6331	1.99	1.94	1.28	1.66	1.95	2.28	2.85
6338	0.99	0.99	0.65	0.84	0.97	1.12	1.39
6341	1.20	1.15	0.81	1.02	1.18	1.36	1.68

Continued on Next Page …

Table 0 – Continued

Trigger	mean(z)	mode(z)	$Q_{5\%}$(z)	$Q_{25\%}$(z)	$Q_{50\%}$(z)	$Q_{75\%}$(z)	$Q_{95\%}$(z)
6342	1.02	0.99	0.65	0.85	0.99	1.16	1.49
6343	1.02	0.99	0.66	0.86	1.00	1.15	1.44
6347	1.20	1.15	0.80	1.01	1.17	1.36	1.68
6354	0.67	0.64	0.42	0.55	0.66	0.78	0.98
6361	0.96	0.96	0.64	0.81	0.95	1.09	1.35
6368	0.69	0.66	0.45	0.58	0.68	0.79	0.98
6372	1.18	1.14	0.79	1.00	1.16	1.34	1.65
6376	1.06	1.00	0.71	0.90	1.04	1.20	1.48
6385	1.09	1.03	0.73	0.93	1.07	1.23	1.51
6386	1.22	1.18	0.83	1.03	1.19	1.37	1.70
6398	1.54	1.50	0.99	1.28	1.51	1.76	2.20
6401	2.01	1.98	1.31	1.69	1.97	2.29	2.82
6411	1.44	1.41	0.94	1.20	1.41	1.65	2.06
6412	1.27	1.23	0.84	1.07	1.24	1.45	1.81
6427	1.08	1.02	0.72	0.92	1.06	1.22	1.51
6436	0.61	0.58	0.39	0.50	0.60	0.71	0.90
6439	1.20	1.16	0.80	1.01	1.18	1.36	1.69
6443	1.36	1.32	0.90	1.14	1.33	1.55	1.93
6445	1.28	1.24	0.86	1.08	1.26	1.45	1.80
6447	1.22	1.18	0.81	1.02	1.19	1.38	1.72
6452	1.36	1.32	0.90	1.13	1.33	1.54	1.91
6462	0.92	0.92	0.61	0.78	0.90	1.04	1.27
6469	1.00	0.99	0.66	0.85	0.99	1.14	1.41
6486	0.63	0.60	0.39	0.51	0.61	0.72	0.92
6488	2.31	2.29	1.51	1.95	2.28	2.63	3.23
6497	2.54	2.53	1.66	2.15	2.51	2.90	3.52
6535	0.83	0.80	0.54	0.70	0.81	0.95	1.17
6540	0.80	0.79	0.50	0.67	0.79	0.92	1.14
6542	0.98	0.99	0.65	0.84	0.96	1.11	1.36
6543	0.81	0.77	0.51	0.67	0.79	0.93	1.18
6547	1.02	0.99	0.68	0.87	1.00	1.15	1.42
6562	1.33	1.29	0.88	1.11	1.30	1.51	1.89
6569	1.32	1.27	0.87	1.10	1.29	1.51	1.88
6571	1.13	1.07	0.74	0.95	1.10	1.28	1.59
6573	1.03	0.99	0.69	0.88	1.01	1.16	1.43
6579	1.36	1.31	0.91	1.14	1.33	1.54	1.91

Continued on Next Page . . .

Table 0 – Continued

Trigger	mean(z)	mode(z)	$Q_{5\%}$(z)	$Q_{25\%}$(z)	$Q_{50\%}$(z)	$Q_{75\%}$(z)	$Q_{95\%}$(z)
6580	1.32	1.27	0.89	1.11	1.29	1.50	1.86
6586	1.36	1.30	0.88	1.12	1.32	1.55	1.96
6591	1.33	1.29	0.90	1.12	1.30	1.51	1.86
6606	0.80	0.78	0.52	0.67	0.78	0.91	1.11
6634	1.94	1.90	1.25	1.62	1.90	2.23	2.78
6635	0.87	0.83	0.54	0.71	0.84	0.99	1.27
6638	1.40	1.36	0.94	1.18	1.37	1.59	1.97
6641	1.34	1.30	0.90	1.13	1.31	1.52	1.90
6643	0.92	0.91	0.60	0.77	0.90	1.04	1.27
6645	0.81	0.79	0.52	0.68	0.80	0.93	1.15
6659	1.09	1.02	0.73	0.92	1.06	1.23	1.53
6662	2.42	2.39	1.59	2.04	2.39	2.76	3.39
6671	0.67	0.64	0.43	0.56	0.66	0.77	0.96
6679	0.75	0.73	0.49	0.63	0.74	0.86	1.06
6682	1.05	1.00	0.70	0.90	1.03	1.19	1.47
6689	0.98	0.98	0.65	0.83	0.96	1.10	1.36
6693	1.07	1.02	0.72	0.91	1.05	1.21	1.49
6697	1.37	1.33	0.92	1.15	1.34	1.55	1.92
6700	0.71	0.68	0.46	0.59	0.70	0.81	1.01
6710	1.75	1.73	1.14	1.47	1.72	1.99	2.45
6715	0.97	0.97	0.65	0.83	0.95	1.09	1.34
6718	1.24	1.18	0.81	1.03	1.21	1.41	1.78
6753	2.66	2.64	1.74	2.24	2.62	3.04	3.71
6757	2.04	2.00	1.33	1.71	2.00	2.32	2.87
6786	1.28	1.24	0.85	1.08	1.26	1.46	1.81
6787	0.93	0.92	0.61	0.79	0.91	1.05	1.28
6788	0.38	0.36	0.24	0.31	0.37	0.44	0.56
6800	0.67	0.64	0.43	0.55	0.65	0.77	0.96
6824	1.06	0.99	0.71	0.90	1.03	1.19	1.49
6866	1.18	1.13	0.78	0.99	1.15	1.33	1.65
6867	1.63	1.58	1.04	1.35	1.59	1.87	2.35
6870	1.75	1.71	1.12	1.45	1.71	2.00	2.49
6904	0.36	0.33	0.22	0.29	0.35	0.41	0.54
6916	0.71	0.68	0.46	0.59	0.69	0.81	1.01
6931	0.70	0.68	0.46	0.59	0.69	0.80	0.99
7009	0.44	0.42	0.28	0.36	0.43	0.51	0.65

Continued on Next Page . . .

Table 0 – Continued

Trigger	mean(z)	mode(z)	$Q_{5\%}(z)$	$Q_{25\%}(z)$	$Q_{50\%}(z)$	$Q_{75\%}(z)$	$Q_{95\%}(z)$
7060	0.80	0.78	0.52	0.67	0.79	0.92	1.13
7063	0.40	0.38	0.25	0.33	0.39	0.46	0.60
7078	0.77	0.75	0.49	0.64	0.75	0.88	1.09
7102	1.03	0.99	0.69	0.88	1.01	1.16	1.42
7106	1.16	1.11	0.78	0.98	1.13	1.31	1.61
7133	1.11	1.05	0.75	0.95	1.09	1.25	1.55
7142	0.92	0.91	0.62	0.78	0.90	1.04	1.27
7148	1.52	1.49	1.00	1.27	1.49	1.73	2.13
7159	1.09	1.00	0.69	0.90	1.06	1.25	1.60
7173	1.01	0.99	0.68	0.86	0.99	1.13	1.40
7187	0.75	0.73	0.48	0.63	0.74	0.86	1.08
7227	0.97	0.98	0.64	0.82	0.95	1.09	1.35
7240	0.77	0.74	0.50	0.64	0.75	0.88	1.09
7281	0.76	0.73	0.48	0.63	0.75	0.88	1.11
7283	1.27	1.23	0.86	1.07	1.24	1.43	1.76
7287	0.65	0.61	0.41	0.53	0.63	0.75	0.96
7290	1.05	0.99	0.70	0.89	1.03	1.19	1.48
7292	0.87	0.86	0.57	0.74	0.86	0.99	1.21
7294	0.76	0.73	0.49	0.63	0.74	0.86	1.07
7297	1.54	1.51	1.02	1.30	1.51	1.75	2.16
7305	0.59	0.56	0.38	0.49	0.58	0.68	0.86
7329	1.23	1.17	0.83	1.03	1.20	1.39	1.73
7344	0.91	0.90	0.60	0.77	0.89	1.03	1.26
7353	0.57	0.54	0.36	0.47	0.55	0.65	0.83
7359	1.06	0.99	0.70	0.90	1.04	1.21	1.51
7361	1.30	1.26	0.86	1.09	1.27	1.47	1.83
7366	0.59	0.56	0.37	0.49	0.58	0.68	0.86
7367	1.63	1.56	1.04	1.34	1.58	1.86	2.35
7375	0.74	0.72	0.48	0.62	0.73	0.85	1.05
7378	0.94	0.93	0.63	0.80	0.92	1.05	1.30
7427	0.59	0.56	0.37	0.49	0.58	0.68	0.86
7430	1.58	1.54	1.04	1.32	1.55	1.80	2.23
7440	0.71	0.69	0.46	0.59	0.70	0.81	1.01
7447	0.67	0.65	0.43	0.56	0.66	0.77	0.97
7449	0.92	0.92	0.60	0.78	0.91	1.05	1.30
7453	1.00	0.99	0.66	0.85	0.99	1.14	1.41

Continued on Next Page . . .

Table 0 – Continued

Trigger	mean(z)	mode(z)	$Q_{5\%}$(z)	$Q_{25\%}$(z)	$Q_{50\%}$(z)	$Q_{75\%}$(z)	$Q_{95\%}$(z)
7455	1.14	1.09	0.76	0.96	1.11	1.29	1.60
7456	0.83	0.80	0.53	0.69	0.81	0.95	1.18
7472	1.19	1.14	0.81	1.01	1.16	1.35	1.66
7495	1.56	1.53	1.02	1.31	1.53	1.78	2.18
7496	1.82	1.80	1.18	1.53	1.79	2.08	2.56
7508	0.79	0.77	0.50	0.66	0.78	0.90	1.11
7514	0.97	0.97	0.63	0.81	0.95	1.11	1.40
7526	1.63	1.59	1.05	1.36	1.59	1.86	2.30
7547	0.81	0.79	0.53	0.68	0.79	0.92	1.13
7554	1.42	1.40	0.94	1.19	1.40	1.62	1.99
7559	1.37	1.32	0.90	1.14	1.34	1.56	1.96
7581	1.65	1.62	1.08	1.38	1.62	1.88	2.33
7584	0.87	0.85	0.56	0.73	0.85	0.99	1.23
7595	1.16	1.11	0.77	0.98	1.13	1.31	1.62
7599	1.12	1.06	0.75	0.95	1.10	1.27	1.58
7601	1.04	0.99	0.70	0.89	1.02	1.18	1.44
7602	0.88	0.86	0.56	0.74	0.86	1.01	1.27
7626	0.73	0.70	0.47	0.61	0.71	0.83	1.03
7663	0.89	0.88	0.58	0.75	0.88	1.01	1.25
7671	0.90	0.88	0.58	0.75	0.89	1.03	1.30
7706	0.75	0.73	0.48	0.63	0.74	0.86	1.06
7710	1.33	1.29	0.89	1.12	1.30	1.51	1.86
7734	1.56	1.53	1.02	1.31	1.53	1.78	2.20
7745	2.34	2.31	1.53	1.97	2.30	2.67	3.29
7753	1.50	1.46	0.99	1.26	1.47	1.71	2.12
7754	0.89	0.89	0.57	0.75	0.88	1.02	1.27
7775	1.09	1.03	0.74	0.93	1.07	1.23	1.52
7784	0.73	0.70	0.46	0.60	0.72	0.84	1.06
7789	0.69	0.66	0.44	0.57	0.67	0.78	0.98
7793	1.07	1.01	0.73	0.92	1.05	1.21	1.50
7800	1.14	1.09	0.76	0.96	1.11	1.29	1.59
7805	2.35	2.31	1.53	1.97	2.31	2.69	3.31
7827	1.39	1.36	0.92	1.16	1.36	1.58	1.96
7830	1.48	1.45	0.98	1.24	1.45	1.69	2.09
7901	0.69	0.66	0.45	0.58	0.68	0.79	0.99
7912	1.22	1.18	0.83	1.03	1.20	1.38	1.71

Continued on Next Page . . .

Table 0 – Continued

Trigger	mean(z)	mode(z)	$Q_{5\%}$(z)	$Q_{25\%}$(z)	$Q_{50\%}$(z)	$Q_{75\%}$(z)	$Q_{95\%}$(z)
7922	0.98	0.99	0.64	0.83	0.96	1.11	1.36
7939	0.90	0.88	0.57	0.74	0.88	1.03	1.31
7943	1.18	1.12	0.80	0.99	1.15	1.33	1.64
7952	1.38	1.34	0.91	1.15	1.35	1.57	1.94
7970	1.30	1.25	0.86	1.09	1.27	1.48	1.85
7979	1.73	1.70	1.12	1.45	1.70	1.97	2.45
7980	1.06	1.00	0.71	0.90	1.04	1.20	1.48
7988	0.76	0.73	0.49	0.64	0.74	0.86	1.06
7995	0.93	0.92	0.62	0.79	0.92	1.05	1.29
7999	1.60	1.58	1.05	1.35	1.57	1.83	2.25
8018	0.61	0.59	0.38	0.50	0.59	0.70	0.89
8027	1.57	1.53	1.03	1.31	1.54	1.79	2.22
8035	1.13	1.07	0.76	0.96	1.10	1.27	1.57
8041	0.92	0.92	0.60	0.77	0.90	1.04	1.28
8047	1.06	1.01	0.72	0.91	1.04	1.19	1.47
8072	1.15	1.10	0.77	0.98	1.12	1.30	1.59
8076	0.76	0.73	0.48	0.63	0.74	0.87	1.07
8077	1.16	1.11	0.77	0.98	1.14	1.32	1.64
8079	1.33	1.30	0.89	1.12	1.31	1.51	1.87
8082	1.22	1.17	0.81	1.03	1.19	1.38	1.72
8085	1.34	1.29	0.90	1.13	1.31	1.52	1.89
8089	0.72	0.69	0.46	0.60	0.70	0.82	1.01
8097	1.88	1.85	1.23	1.58	1.85	2.14	2.64
8104	0.65	0.62	0.42	0.54	0.64	0.74	0.93
8120	1.39	1.35	0.93	1.17	1.36	1.57	1.94

Notes: The column denoted by 'Trigger' contains the trigger IDs of BATSE SGRBs. The columns denoted by mean(z), mode(z) represent the mean and the most likely values of redshifts respectively. The columns denoted by $Q_{5\%}$(z), $Q_{25\%}$(z), $Q_{50\%}$(z), $Q_{75\%}$(z), $Q_{95\%}$(z) represent the corresponding percentage quantiles of the redshift PDF for each SGRB. For example, $Q_{50\%}$(z) represents the median redshift of each SGRB.

Bibliography

Abbott, Benjamin P et al. (2017). "GW170817: observation of gravitational waves from a binary neutron star inspiral". In: *Physical Review Letters* 119.16, p. 161101.

Ashcraft, Teresa and Bradley E Schaefer (2007). "Are There Any Redshift> 8 Gamma-Ray Bursts in the BATSE Catalog?" In: *The Astrophysical Journal* 671.2, p. 1896.

Atwood, WB et al. (2009). "The large area telescope on the Fermi gamma-ray space telescope mission". In: *The Astrophysical Journal* 697.2, p. 1071.

Backus, John (1978). "The history of Fortran I, II, and III". In: *ACM Sigplan Notices* 13.8, pp. 165–180.

Band, D et al. (1993). "BATSE observations of gamma-ray burst spectra. I-Spectral diversity". In: *The Astrophysical Journal* 413, pp. 281–292.

Band, David L and Robert D Preece (2005). "Testing the gamma-ray burst energy relationships". In: *The Astrophysical Journal* 627.1, p. 319.

Berger, Edo, W Fong, and R Chornock (2013). "An r-process kilonova associated with the short-hard GRB 130603B". In: *The Astrophysical Journal Letters* 774.2, p. L23.

Bernardini, Maria Grazia et al. (2014). "Comparing the spectral lag of short and long gamma-ray bursts and its relation with the luminosity". In: *Monthly Notices of the Royal Astronomical Society* 446.2, pp. 1129–1138.

Blinnikov, SI et al. (2018). "Exploding neutron stars in close binaries". In: *arXiv preprint arXiv:1808.05287*.

Bloom, Joshua S, Shrinivas R Kulkarni, and S George Djorgovski (2002). "The observed offset distribution of gamma-ray bursts from their host galaxies: a robust clue to the nature of the progenitors". In: *The Astronomical Journal* 123.3, p. 1111.

Bloom, Joshua S, JX Prochaska, et al. (2006). "Closing in on a short-hard burst progenitor: constraints from early-time optical imaging and spectroscopy of a possible host galaxy of GRB 050509b". In: *The Astrophysical Journal* 638.1, p. 354.

Bloom, JS et al. (2009). "Observations of the naked-eye GRB 080319B: implications of nature's brightest explosion". In: *The Astrophysical Journal* 691.1, p. 723.

Butler, Nathaniel R, Joshua S Bloom, and Dovi Poznanski (2010). "The cosmic rate, luminosity function, and intrinsic correlations of long gamma-ray bursts". In: *The Astrophysical Journal* 711.1, p. 495.

Butler, Nathaniel R, Daniel Kocevski, and Joshua S Bloom (2009). "Generalized tests for selection effects in gamma-ray burst high-energy correlations". In: *The Astrophysical Journal* 694.1, p. 76.

Butler, Nathaniel R, Daniel Kocevski, Joshua S Bloom, and Jason L Curtis (2007). "A complete catalog of Swift gamma-ray burst spectra and durations: demise of a physical origin for pre-Swift high-energy correlations". In: *The Astrophysical Journal* 671.1, p. 656.

Dainotti, Maria Giovanna et al. (2015). "Selection effects in gamma-ray burst correlations: consequences on the ratio between gamma-ray burst and star formation rates". In: *The Astrophysical Journal* 800.1, p. 31.

Dainotti, Maria et al. (2019). "Gamma-ray Bursts as distance indicators through a machine learning approach". In: *arXiv preprint arXiv:1907.05074*.

Dempster, Arthur P, Nan M Laird, and Donald B Rubin (1977). "Maximum likelihood from incomplete data via the EM algorithm". In: *Journal of the royal statistical society. Series B (methodological)*, pp. 1–38.

Fenimore, Ed E and E Ramirez-Ruiz (2000). "Redshifts for 220 batse gamma-ray bursts determined by variability and the cosmological consequences". In: *arXiv preprint astro-ph/0004176*.

Firmani, C et al. (2006). "Discovery of a tight correlation among the prompt emission properties of long gamma-ray bursts". In: *Monthly Notices of the Royal Astronomical Society* 370.1, pp. 185–197.

Fishman, Gerald J and Charles A Meegan (1995). "Gamma-ray bursts". In: *Annual Review of Astronomy and Astrophysics* 33.1, pp. 415–458.

Fishman, Gerald J, Charles A Meegan, et al. (1994). "The first BATSE gamma-ray burst catalog". In: *The Astrophysical Journal Supplement Series* 92, pp. 229–283.

Fishman, GJ et al. (1985). "Burst and Transient Source Experiment (BATSE) for the Gamma Ray Observatory (GRO)". In:

Frail, Dale A et al. (2001). "Beaming in gamma-ray bursts: evidence for a standard energy reservoir". In: *The Astrophysical Journal Letters* 562.1, p. L55.

Gehrels, Neil et al. (2004). "The Swift gamma-ray burst mission". In: *The Astrophysical Journal* 611.2, p. 1005.

Ghirlanda, G et al. (2008). "The E peak–E iso plane of long gamma-ray bursts and selection effects". In: *Monthly Notices of the Royal Astronomical Society* 387.1, pp. 319–330.

Goldstein, Adam et al. (2013). "The BATSE 5B gamma-ray burst spectral catalog". In: *The Astrophysical Journal Supplement Series* 208.2, p. 21.

Guidorzi, Cristiano (2005). "Testing the gamma-ray burst variability/peak luminosity correlation using the pseudo-redshifts of a large sample of BATSE gamma-ray bursts". In: *Monthly Notices of the Royal Astronomical Society* 364.1, pp. 163–168.

Haario, Heikki, Eero Saksman, Johanna Tamminen, et al. (2001). "An adaptive Metropolis algorithm". In: *Bernoulli* 7.2, pp. 223–242.

Hakkila, Jon et al. (2003). "How sample completeness affects gamma-ray burst classification". In: *The Astrophysical Journal* 582.1, p. 320.

Jarosik, N et al. (2011). "Seven-year wilkinson microwave anisotropy probe (WMAP*) observations: sky maps, systematic errors, and basic results". In: *The Astrophysical Journal Supplement Series* 192.2, p. 14.

Katz, JI (1993). "Low frequency spectra of gamma-ray bursts". In: *arXiv preprint astro-ph/9312034*.

Klebesadel, Ray W, Ian B Strong, and Roy A Olson (1973). "Observations of gamma-ray bursts of cosmic origin". In: *The Astrophysical Journal* 182, p. L85.

Kouveliotou, Chryssa et al. (1993). "Identification of two classes of gamma-ray bursts". In: *The Astrophysical Journal* 413, pp. L101–L104.

Kumbhare, Shashank and Amir Shahmoradi (2020). "Parallel Adapative Monte Carlo Optimization, Sampling, and Integration in C/C++, Fortran, MATLAB, and Python". In: *Bulletin of the American Physical Society*.

Lattimer, James M and David N Schramm (1976). "Tidal Disruption Of Neutron Stars By Black-Holes In Close Binaries". In:

Lazzati, Davide et al. (2013). "Photospheric emission as the dominant radiation mechanism in long-duration gamma-ray bursts". In: *The Astrophysical Journal* 765.2, p. 103.

Lien, Amy et al. (2016). "The third Swift burst alert telescope gamma-ray burst catalog". In: *The Astrophysical Journal* 829.1, p. 7.

Lloyd, Nicole M and Vahé Petrosian (1999). "Distribution of spectral characteristics and the cosmological evolution of gamma-ray bursts". In: *The Astrophysical Journal* 511.2, p. 550.

Lloyd, Nicole M, Vahé Petrosian, and Robert S Mallozzi (2000). "Cosmological versus Intrinsic: The Correlation between Intensity and the Peak of the $\nu F\nu$ Spectrum of Gamma-Ray Bursts". In: *The Astrophysical Journal* 534.1, p. 227.

MacFadyen, Andrew I, SE Woosley, and A Heger (2001). "Supernovae, jets, and collapsars". In: *The Astrophysical Journal* 550.1, p. 410.

Meegan, Charles et al. (2009). "The Fermi gamma-ray burst monitor". In: *The Astrophysical Journal* 702.1, p. 791.

Metcalf, Michael, John Reid, and Malcolm Cohen (2011). *Modern Fortran Explained*. Oxford University Press.

Nakar, Ehud (2007). "Short-hard gamma-ray bursts". In: *Physics Reports* 442.1-6, pp. 166–236.

Nakar, Ehud and Tsvi Piran (2004). "Outliers to the isotropic energy-Peak energy relation in GRBs". In: *Mon. Not. Roy. Astron. Soc.* 360.astro-ph/0412232, p. 73.

Nava, Lara et al. (2008). "Peak energy of the prompt emission of long gamma-ray bursts versus their fluence and peak flux". In: *Monthly Notices of the Royal Astronomical Society* 391.2, pp. 639–652.

Paciesas, William S et al. (1999). "The fourth BATSE gamma-ray burst catalog (revised)". In: *The Astrophysical Journal Supplement Series* 122.2, p. 465.

Peebles, Phillip James Edwin (1993). *Principles of physical cosmology*. Princeton university press.

Perna, Rosalba, Re'em Sari, and Dale Frail (2003). "Jets in gamma-ray bursts: tests and predictions for the structured jet model". In: *The Astrophysical Journal* 594.1, p. 379.

Petrosian, Vahe', Nicole M Lloyd-Ronning, and Andrew Lee (1999). "Cosmological signatures in temporal and spectral characteristics of gamma-ray bursts". In: *arXiv preprint astro-ph/9906393*.

Petrosian, Vahé, Ellie Kitanidis, and Daniel Kocevski (2015). "Cosmological evolution of long gamma-ray bursts and the star formation rate". In: *The Astrophysical Journal* 806.1, p. 44.

Petrosian, Vahé and Theodore T Lee (1996). "The Fluence distribution of gamma-ray bursts". In: *The Astrophysical Journal Letters* 467.1, p. L29.

Podsiadlowski, Ph et al. (2004). "The rates of hypernovae and gamma-ray bursts: implications for their progenitors". In: *The Astrophysical Journal Letters* 607.1, p. L17.

Pontzen, Andrew et al. (2010). "The nature of H i absorbers in gamma-ray burst afterglows: clues from hydrodynamic simulations". In: *Monthly Notices of the Royal Astronomical Society* 402.3, pp. 1523–1535.

Prochaska, Jason X et al. (2006). "The galaxy hosts and large-scale environments of short-hard gamma-ray bursts". In: *The Astrophysical Journal* 642.2, p. 989.

Reichart, Daniel E et al. (2001). "A possible cepheid-like luminosity estimator for the long gamma-ray bursts". In: *The Astrophysical Journal* 552.1, p. 57.

Rizzuto, D et al. (2007). "Testing the gamma-ray burst variability/peak luminosity correlation on a Swift homogeneous sample". In: *Monthly Notices of the Royal Astronomical Society* 379.2, pp. 619–628.

Robbins, Herbert (1985). "An empirical Bayes approach to statistics". In: *Herbert Robbins Selected Papers*. Springer, pp. 41–47.

Schaefer, Bradley E, Ming Deng, and David L Band (2001). "Redshifts and luminosities for 112 gamma-ray bursts". In: *The Astrophysical Journal Letters* 563.2, p. L123.

Shahmoradi, A. and R. J. Nemiroff (Dec. 2017a). *LgrbWorldModel: Long-duration Gamma-Ray Burst World Model*. Astrophysics Source Code Library. ascl: `1712.016`.

— (Dec. 2017b). *SgrbWorldModel: Short-duration Gamma-Ray Burst World Model*. Astrophysics Source Code Library. ascl: `1712.015`.

— (2011a). "The possible impact of gamma-ray burst detector thresholds on cosmological standard candles". In: *Monthly Notices of the Royal Astronomical Society* 411.3, pp. 1843–1856.

— (2011b). "VizieR Online Data Catalog: Gamma-ray bursts spectral peak estimator (Shahmoradi+, 2010)". In: *VizieR Online Data Catalog* 740.

Shahmoradi, Amir (2013a). "A Multivariate Fit Luminosity Function and World Model for Long Gamma-Ray Bursts". In: *The Astrophysical Journal* 766.2, p. 111.

— (2013b). "Gamma-Ray bursts: Energetics and Prompt Correlations". In: *arXiv preprint arXiv:1308.1097*.

— (2014). "On the similarities of the prompt gamma-ray emissions in Short and Long Gamma-Ray Busts". In: *APS April Meeting Abstracts*.

— (2017). "Multilevel Bayesian Parameter Estimation in the Presence of Model Inadequacy and Data Uncertainty". In: *arXiv preprint arXiv:1711.10599*.

— (2018). "Multilevel Bayesian Analysis of Biophysical Data in the Presence of Model Inadequacy and Measurement Error". In: *Bulletin of the American Physical Society*.

— (2019). "ParaMonte: A user-friendly parallel Monte Carlo optimization, sampling, and integration library for scientific inference". In: *Bulletin of the American Physical Society*.

Shahmoradi, Amir, Fatemeh Bagheri, and Shashank Kumbhare (2020). "ParaMonte: Plain Powerful Parallel Monte Carlo Library". In: *Bulletin of the American Physical Society*.

Shahmoradi, Amir and RJ Nemiroff (2011). "A Cosmological Discriminator Designed to Avoid Selection Bias". In: *Bulletin of the American Astronomical Society*. Vol. 43.

— (2014). "Classification and Energetics of Cosmological Gamma-Ray Bursts". In: *American Astronomical Society Meeting Abstracts# 223*. Vol. 223.

Shahmoradi, Amir and Robert Nemiroff (2009). "How Real detector thresholds create false standard candles". In: *AIP Conference Proceedings*. Vol. 1133. 1. AIP, pp. 425–427.

Shahmoradi, Amir and Robert J Nemiroff (2010). "Hardness as a spectral peak estimator for gamma-ray bursts". In: *Monthly Notices of the Royal Astronomical Society* 407.4, pp. 2075–2090.

— (2015). "Short versus long gamma-ray bursts: a comprehensive study of energetics and prompt gamma-ray correlations". In: *Monthly Notices of the Royal Astronomical Society* 451.1, pp. 126–143.

— (2019). "A Catalog of Redshift Estimates for 1366 BATSE Long-Duration Gamma-Ray Bursts: Evidence for Strong Selection Effects on the Phenomenological Prompt Gamma-Ray Correlations". In: *arXiv preprint arXiv:1903.06989*.

Tanvir, NR et al. (Aug. 2013). "A kilonova associated with short-duration gamma-ray burst 130603B." In: *Nature* 500.7464, pp. 547–549. ISSN: 1476-4687. DOI: `10.1038/nature12505`. URL: `http://dx.doi.org/10.1038/nature12505`.

Tavani, M (1996). "A shock emission model for gamma-ray bursts. II. Spectral properties". In: *The Astrophysical Journal* 466, p. 768.

Watson, Darach et al. (2006). "Are short γ-ray bursts collimated? GRB 050709, a flare but no break". In: *Astronomy & Astrophysics* 454.3, pp. L123–L126.

Wickramasinghe, T and TN Ukwatta (2010). "An analytical approach for the determination of the luminosity distance in a flat universe with dark energy". In: *Monthly Notices of the Royal Astronomical Society* 406.1, pp. 548–550.

Winberg, S (1972). "Gravitation and cosmology". In: *ed. John Wiley and Sons, New York*.

Woosley, SE and JS Bloom (2006). "The supernova–gamma-ray burst connection". In: *Annu. Rev. Astron. Astrophys.* 44, pp. 507–556.

Woźniak, PR et al. (2009). "Gamma-Ray Burst at the extreme:"the naked-eye burst" GRB 080319B". In: *The Astrophysical Journal* 691.1, p. 495.

Xiao, Limin and Bradley E Schaefer (2009). "Estimating redshifts for long gamma-ray bursts". In: *The Astrophysical Journal* 707.1, p. 387.

Yonetoku, Daisuke, Toshio Murakami, et al. (2004). "Gamma-ray burst formation rate inferred from the spectral peak energy-peak luminosity relation". In: *The Astrophysical Journal* 609.2, p. 935.

Yonetoku, Daisuke, Takashi Nakamura, et al. (2014). "Short Gamma-Ray Burst Formation Rate from BATSE Data Using Ep-Lp Correlation and the Minimum Gravitational-wave Event Rate of a Coalescing Compact Binary". In: *The Astrophysical Journal* 789.1, p. 65.

Zhang, Bin-Bin et al. (2014). "How long does a burst burst?" In: *The Astrophysical Journal* 787.1, p. 66.